Article

Double-Loop PID-Type Neural Network Sliding Mode Control of an Uncertain Autonomous Underwater Vehicle Model Based on a Nonlinear High-Order Observer with Unknown Disturbance

Jiajian Liang, Wenkai Huang *, Fobao Zhou, Jiaqiao Liang, Guojian Lin, Endong Xiao, Hongquan Li and Xiaolin Zhang

School of Mechanical and Electrical Engineering, Guangzhou University, Guangzhou 510006, China
* Correspondence: smallkat@gzhu.edu.cn

Abstract: An unknown nonlinear disturbance seriously affects the trajectory tracking of autonomous underwater vehicles (AUVs). Thus, it is critical to eliminate the influence of such disturbances on AUVs. To address this problem, this paper proposes a double-loop proportional–integral–differential (PID) neural network sliding mode control (DLNNSMC). First, a double-loop PID sliding mode surface is proposed, which has a faster convergence speed than other PID sliding mode surfaces. Second, a nonlinear high-order observer and a neural network are combined to observe and compensate for the nonlinear disturbance of the AUV system. Then, the bounded stability of an AUV closed-loop system is analyzed and demonstrated using the Lyapunov method, and the time-domain method is used to verify that the velocity- and position-tracking errors of AUVs converge to zero exponentially. Finally, the radial basis function (RBF) neural network PID sliding mode control (RBFPIDSMC) and the RBF neural network PID sliding mode control (RBFPDSMC) are compared with this method in two trajectory tracking control simulation experiments. In the first experiment, the average Euclidean distance of the position-tracking error for this method was reduced by approximately 73.6% and 75.3%, respectively, compared to those for RBFPDSMC and RBFPIDSMC. In the second experiment, the average Euclidean distance of the position tracking error for this method was reduced by approximately 86.8% and 88.8%, respectively. The two experiments showed that the proposed control method has a strong anti-jamming ability and tracking effect. The simulation results obtained in the Gazebo environment validated the superiority of this method.

Keywords: autonomous underwater vehicles (AUVs); PID sliding mode surface; neural network; observer; sliding mode control

MSC: 70E60

1. Introduction

In the past decades, considerable progress has been made in submarine engineering technology in fields such as oceanographic observations, undersea oil detection, geological sampling, deep-sea archaeology, and minesweeping [1–4]. Autonomous underwater vehicles (AUVs) have become the most popular solution for many submarine missions. Trajectory tracking control is an important part of the abovementioned applications. However, due to the complex hydrodynamic characteristics of AUVs, especially the inherent high nonlinearity, strong coupling, and time-varying and uncertain characteristics of fully actuated AUVs, and the existence of time-varying external disturbances [5,6], which are chaotic and difficult to measure or estimate in an underwater environment, the AUV trajectory is difficult to track. Therefore, a control method that can address the inherent nonlinear dynamics, imprecise model parameters, and time-varying external disturbances of AUVs is required.

The problem of inherent nonlinear dynamics has been extensively researched. The proportional–integral–differential (PID) control consists of proportional, integral, and differential terms and does not need to establish a nonlinear dynamic model for the control object. Therefore, PID control can be applied to nonlinear systems and has been widely used for AUV trajectory tracking control [7–9]. However, for complex underwater trajectory tracking, PID control cannot provide accurate tracking. Moreover, as Kim et al. [9] indicated, PID control can only provide set-point regulation if the disturbances are constant. Many engineers and researchers have significantly contributed to improving the tracking accuracy of the AUV trajectory and to enhancing the robustness to dynamic uncertainties and time-varying ocean disturbances. So far, many advanced control methods have been proposed for AUV trajectory tracking, including backward control [10–12], adaptive control [13,14], neural network control [15–17], model predictive control [18], boundary control [19–21], and sliding mode control (SMC) [22–25]. Of these, SMC has attracted much attention due to its excellent and concise characteristics. Because of its strong robustness in relation to model uncertainty and the suppression of external interference, SMC is highly suitable for AUV trajectory tracking control in a complex ocean environment. However, the design of a traditional SMC uses a linear sliding surface, a discontinuous symbolic function, and an assumed uncertainty upper-bound value. Thus, the application of the traditional SMC can easily cause a slow response, and the position tracking error cannot converge in limited time when applied to AUV trajectory tracking control.

To overcome the shortcomings of SMC, many advanced technologies have been proposed. For example, Guerrero used the high-order sliding mode control (HOSMC) to address the chattering phenomenon of AUVs in trajectory tracking control [26]; however, HOSMC cannot facilitate the convergence of the AUV trajectory tracking error to a smaller bounded area within limited time. Terminal SMC (TSMC) can overcome finite-time tracking [27]. However, in this control method, all tracking errors can only be guaranteed to be bounded and require an upper bound of parameter uncertainty, which is difficult to obtain in practical engineering. Wang proposed an adaptive non-singular terminal sliding mode control (ANTSMC) method for the 3D trajectory tracking control of AUVs [28]. Because of the use of an adaptive algorithm, this method does not require an upper bound of parameter uncertainty. Compared to TSMC, this method enhances the system robustness and overcomes the drawbacks of SMC. However, this method does not facilitate the convergence of the errors to the neighborhood of zero, although it guarantees boundedness between the position and the speed tracking errors. Although the aforementioned improved SMC overcomes the shortcomings of the traditional SMC and obtains effective solutions, in the actual application of AUV trajectory tracking control, the AUV system must solve the respective problems of HOSMC, TSMC, and ANTSMC simultaneously.

To address the above problems, Chen proposed a PID sliding mode surface [29], which has the advantages of both PID control and SMC, with a fast convergence speed and strong robustness. However, the speed and position tracking errors cannot be converged simultaneously. Based on [29], this paper proposes a double-loop PID sliding mode surface to compensate for the disadvantage of the PID sliding mode surface and design a new double-loop neural network PID sliding mode control (DLNNSMC) method based on a nonlinear high-order observer so that the position and velocity tracking errors of the AUV trajectory tracking control can converge to zero in limited time. However, this method has a breakthrough point: the control law requires an accurate dynamic model and its derivation. An accurate dynamic model is difficult to derive in research and development. To solve this problem, in this study, a radial basis function (RBF) neural network was used to approximate the AUV dynamic model. This neural network has been widely used in trajectory tracking control [30,31] and can fit many functions well. In addition, we designed a high-order nonlinear observer to compensate for the disturbance of the AUV dynamic model caused by complex external currents and model uncertainty in the differential terms of the PID sliding surface. Moreover, since the high-order nonlinear observer is a supplement to the uncertainties, the control law does not need to assume the

upper bound of parameter uncertainty. The main contributions of the proposed control method are as follows:

(1) The proposed double-loop PID sliding surface can make the speed and position tracking errors of the AUV trajectory tracking control converge to the neighborhood of zero in limited time.

(2) In the control design, a high-order nonlinear observer is presented, which compensates for the disturbance caused by complex external currents and model uncertainty in the AUV dynamic model in the differential term of the PID sliding surface. In addition, there is no need to depend on the dynamic model differentiation caused by the inner-loop PID sliding mode surface; we only need to use the neural network strategy to obtain a fast approximation and realize the practicability of the proposed control law.

(3) The convergence of the velocity and position tracking errors to the neighborhood of zero is proved by the Lyapunov method and time-domain method, respectively.

2. AUV Modeling

Figure 1 shows the markers for the Earth-fixed (EF) frame and underwater vehicle Body-fixed (BF) frame. The linear and angular velocities of the BF frame can be expressed as $v = [u, v, w, p, q, r]^T \in R^{6 \times 1}$, and those of the EF frame can be expressed as $\dot{\eta}$, where $\eta = [x, y, z, \varphi, \Theta, \psi]^T \in R^{6 \times 1}$.
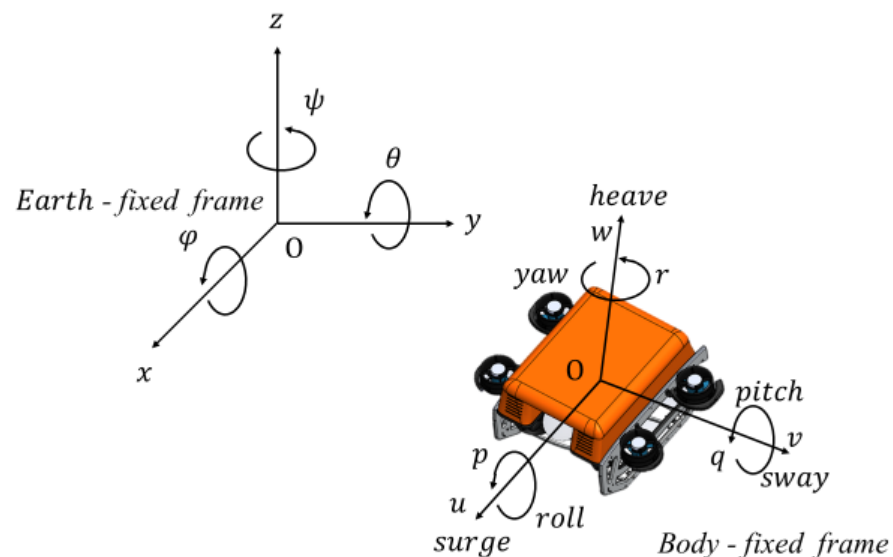

Figure 1. Autonomous underwater vehicles (AUVs) in Body-fixed and Earth-fixed frames.

The body velocity v of an object can be converted to the inertial velocity $\dot{\eta}$ by using the following kinematic equation:

$$\dot{\eta} = J(\eta) \tag{1}$$

where $J(\eta) \in R^{6 \times 6}$ is in the form of a Jacobian matrix:

$$J(\eta) = \begin{bmatrix} J_1(\eta_1) & 0_{3 \times 3} \\ 0_{3 \times 3} & J_2(\eta_2) \end{bmatrix}. \tag{2}$$

$J_1(\eta): R^6 \to R^{3 \times 3}$ and $J_2(\eta): R^6 \to R^{3 \times 3}$ are defined as

$$J_1(\eta_1) = \begin{pmatrix} c\psi c\Theta & -s\psi c\varphi + s\Theta s\varphi c\psi & s\psi s\varphi + c\psi c\varphi s\Theta \\ s\psi c\Theta & c\psi c\varphi + s\psi s\varphi s\Theta & -c\psi s\varphi + s\psi c\varphi s\Theta \\ -s\Theta & c\Theta s\varphi & c\Theta c\varphi \end{pmatrix}, \tag{3}$$

$$J_2(\eta_2) = \begin{pmatrix} 1 & s\varphi t\Theta & c\varphi t\Theta \\ 0 & c\varphi & -s\varphi \\ 0 & s\varphi/c\Theta & c\varphi/c\Theta \end{pmatrix}, \tag{4}$$

where s (·), c (·), and t (·) are abbreviations of sin (·), cos (·), and tan (·), respectively.

The AUV dynamics in the BF frame are expressed as

$$M\dot{v} + C(v)v + D(v)v + g(\eta) = \tau + \tau_d, \tag{5}$$

where $M \in R^{6\times6}$ is the inertia matrix; $C(v) \in R^{6\times6}$ is the Coriolis matrix and centripetal matrix; $D(v) \in R^{6\times6}$ is the damping matrix; $g(\eta) \in R^6$ is the restoring force and moment matrix; $\tau \in R^6$ represents the virtual forces and moments; and $\tau_d \in R^6$ represents the model uncertainty effects.

In many practical applications, an AUV dynamic model cannot be obtained accurately. Therefore, the coefficient matrix in the AUV dynamic model (5) is divided into a standard part and an uncertainty part:

$$\begin{aligned} M &= \hat{M} + \overline{M} \\ C(v) &= \hat{C}(v) + \overline{C}(v) \\ D(v) &= \hat{D}(v) + \overline{D}(v) \\ g(\eta) &= \hat{g}(\eta) + \overline{g}(\eta), \end{aligned} \tag{6}$$

where $\hat{M}$, $\hat{C}(v)$, $\hat{D}(v)$, and $\hat{g}(\eta)$ are standard terms, and $\overline{M}$, $\overline{C}(v)$, $\overline{D}(v)$, and $\overline{g}(\eta)$ are interference terms.

Now, the AUV dynamic model can be rewritten as

$$\hat{M}\dot{v} + \hat{C}(v)v + \hat{D}(v)v + \hat{g}(\eta) = \tau + \tau_{d\eta}, \tag{7}$$

where $\tau_{d\eta}$ is expressed as lumped system uncertainty:

$$\tau_{d\eta} = -\overline{M}\dot{v} - \overline{C}(v)v - \overline{D}(v)v - \overline{g}(\eta) - \tau_d. \tag{8}$$

3. Controller Design

3.1. Preliminaries

We now provide the related lemmas and assumptions for facilitating the subsequent analysis and design.

Lemma 1 [19]. *Let* $\omega_1(x,t)$, $\omega_2(x,t) \in R$, *with* $(x,t) \in [0, L] \times [0, +\infty)$; *then, there exists* $\sigma > 0$ *such that*

$$\omega_1(x,t)\omega_2(x,t) \leq \frac{1}{\sigma}\omega_1^2(x,t) + \sigma\omega_2^2(x,t). \tag{9}$$

3.2. DLNNSMC Scheme

Figure 2 shows a schematic of the proposed DLNNSMC scheme for AUVs. Considering the time-varying reference trajectories $\eta_d \in R^6$, we define the position tracking error as $\tilde{\eta} = \eta - \eta_d$ and, after combining with (1), we obtain

$$\dot{\tilde{\eta}} = J(\eta)v - \dot{\eta}_d. \tag{10}$$

Then, we define the surface of the speed-tracking error as

$$S_{\tilde{v}} = v - v_c. \tag{11}$$

To convert $S_{\tilde{v}}$ into a PID sliding surface, the virtual speed control command $v_c \in R^6$ is obtained as follows:

$$v_c = J^{-1}(\eta)\dot{\eta}_d - J^{-1}(\eta)\left(K_1\tilde{\eta} + K_2\int_0^t \tilde{\eta}dt\right), \tag{12}$$

where $K_1 = \mathrm{diag}[k_{11}, k_{12}, \ldots, k_{16}] \in R^{6\times 6}$ and $K_2 = \mathrm{diag}[k_{21}, k_{22}, \ldots, k_{26}] \in R^{6\times 6}$ are constant positive-definite matrices that need to be designed, and k_{1i}, k_{2i} $(i = 1, \ldots, 6)$ satisfies the discriminant $k_{1i}^2 - 4k_{2i} \geq 0$ of the quadratic equation of one variable. Combining (11) and (12), an outer-loop PID sliding surface is designed:

$$S_{\tilde{v}} = \dot{\tilde{\eta}} + K_1\tilde{\eta} + K_2\int_0^t \tilde{\eta}dt. \tag{13}$$
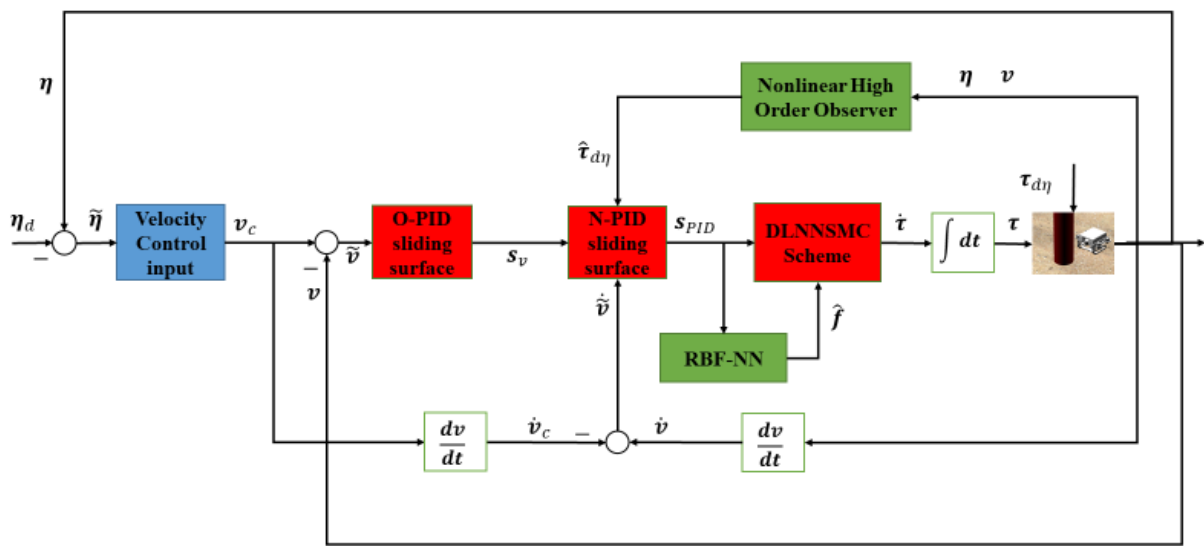

Figure 2. Structural framework of the double-loop neural network proportional–integral–derivative (PID) sliding mode control scheme.

Based on (13), an inner-loop PID sliding surface is designed:

$$S_{PID} = K_P S_{\tilde{v}} + K_i\int_0^t S_{\tilde{v}}dt + K_d\frac{dS_{\tilde{v}}}{dt}, \tag{14}$$

where $K_P = \mathrm{diag}[k_{P1}, k_{P2}, \ldots, k_{P6}] \in R^{6\times 6}$, $K_I = \mathrm{diag}[k_{I1}, \ldots, \ldots, k_{I6}] \in R^{6\times 6}$, and $K_D = \mathrm{diag}[k_{D1}, k_{D2}, \ldots, k_{D6}]$ are the diagonal matrices of the proportional, integral, and differential gain coefficients, respectively.

From (7), the differential of v can be expressed as

$$\frac{dv}{dt} = \hat{M}^{-1}\left(\tau + \tau_{d\eta} - \hat{C}(v)v - \hat{D}(v)v - \hat{g}(\eta)\right). \tag{15}$$

Differentiating (11) and combining it with (15), we obtain

$$\frac{dS_{\tilde{v}}}{dt} = \frac{dv}{dt} - \frac{dv_c}{dt} = \hat{M}^{-1}\left(\tau + \tau_{d\eta} - \hat{C}(v)v - \hat{D}(v)v - \hat{g}(\eta)\right) - \dot{v}_c. \tag{16}$$

Substituting (16) into (14), we obtain

$$S_{PID} = K_P S_{\tilde{v}} + K_i\int_0^t S_{\tilde{v}}dt + K_d\left[\hat{M}^{-1}\left(\tau_{d\eta} - \hat{C}(v)v - \hat{D}(v)v - \hat{g}(\eta)\right) - \dot{v}_c + \hat{M}^{-1}\tau\right]. \tag{17}$$

S_{PID} can be differentiated as follows:

$$
\begin{aligned}
\dot{S}_{PID} = \ & K_P \dot{S}_{\tilde{v}} + K_i S_{\tilde{v}} + K_d \left[\hat{M}^{-1} \left(\dot{\tau}_{d\eta} - \dot{\hat{C}}(v)v - \hat{C}(v)\dot{v} - \dot{\hat{D}}(v)v - \hat{D}(v)\dot{v} - \dot{\hat{g}}(\eta) \right) - \ddot{v}_c + \hat{M}^{-1}\dot{\tau} \right] \\
= \ & -\left\{ -K_P \dot{S}_{\tilde{v}} - K_i S_{\tilde{v}} + K_d \left[\hat{M}^{-1} \left(\dot{\hat{C}}(v)v + \hat{C}(v)\dot{v} + \dot{\hat{D}}(v)v + \hat{D}(v)\dot{v} + \dot{\hat{g}}(\eta) \right) + \ddot{v}_c \right] \right\} + \\
& K_d \hat{M}^{-1}\dot{\tau} + K_d \hat{M}^{-1}\dot{\tau}_{d\eta}
\end{aligned}
\tag{18}
$$

Let $f = -K_P \dot{S}_{\tilde{v}} - K_i S_{\tilde{v}} + K_d \left[\hat{M}^{-1} \left(\dot{\hat{C}}(v)v + \hat{C}(v)\dot{v} + \dot{\hat{D}}(v)v + \hat{D}(v)\dot{v} + \dot{\hat{g}}(\eta) \right) + \ddot{v}_c \right] +$
$K_d \hat{M}^{-1}\dot{\tau}_{d\eta}$ be a lumped unknown function, and $G = K_d \hat{M}^{-1}$. Then, (18) can be simplified as

$$
\dot{S}_{PID} = -f + G\dot{\tau}.
\tag{19}
$$

The Gaussian RBFNN [30,32] possesses the function approximation ability and has been widely utilized in the control of complex nonlinear systems with uncertainties. In this paper, six identical RBFNNs were designed; Figure 3 shows the schematic of the RBFNN structure. The unknown function f to be approximated can be described as

$$
f = W^{*T}\phi(S_{PID}) - \varepsilon,
\tag{20}
$$

where $\phi(S_{PID}) \in R^{30}$, $S_{PID} = [S_{PID1}, S_{PID2}, \ldots, S_{PID6}]$ is a neural network input vector, $W^* = [W_1^*, W_2^*, \ldots, W_6^*]^T$ is an ideal weight vector, $W_i^* = [W_{i1}^*, W_{i2}^*, \ldots, W_{i5}^*]^T (i = 1 \cdots 6, 5$ is the number of hidden nodes), and $\phi(S_{PID}) = [\phi_1(S_{PID1}), \phi_2(S_{PID2}), \ldots, \phi_6(S_{PID6})]^T$ is a vector with a basic function $\phi_i(S_{PIDi}) = [\phi_{i1}(S_{PIDi}), \phi_{i2}(S_{PIDi}), \ldots, \phi_{i5}(S_{PIDi})]^T$. In addition, $\varepsilon = [\varepsilon_1, \varepsilon_2, \ldots, \varepsilon_6]^T$ is a vector of bounded approximation errors. Therefore, we have $\varepsilon \leq \bar{\varepsilon}$ and $\bar{\varepsilon} > 0$. The Gaussian RBF considered in this paper is expressed as follows:

$$
\begin{aligned}
\phi_{ik}(s_i) = \ & \exp\left[\frac{(s_i - c_{ik})^T(s_i - c_{ik})}{b_{ik}^2} \right] \\
& i = 1, 2, \ldots, 6, k = 1, 2, \ldots, 5,
\end{aligned}
\tag{21}
$$

where c_{ik} and b_{ik} represent the center and the width of the Gaussian function, respectively.
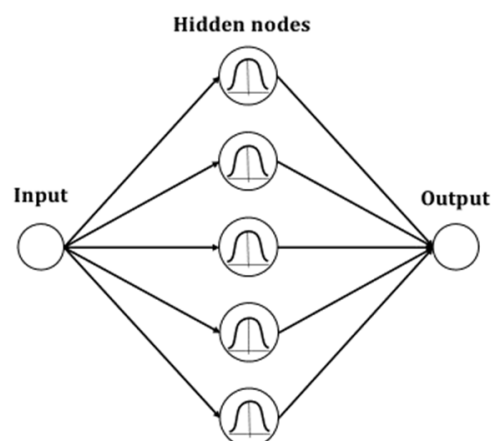

Figure 3. Structural diagram of the radial basis function with one hidden layer.

The vector of the estimated weight is expressed as

$$
\hat{W} = W^* + \widetilde{W},
\tag{22}
$$

where $\widetilde{W}$ represents the error vector of the estimated weight.

Setting the unknown function $f \in R^6$ as the RBF output, the approximate value of f can be expressed as

$$\hat{f} = \hat{W}^T \phi(S_{PID}). \tag{23}$$

The design method of the proposed SMC law can be expressed as follows:

$$\dot{\tau} = \frac{1}{G}(\hat{f} - KS_{PID}), \tag{24}$$

where $K = \text{diag}[K_1, K_2, \ldots, K_6]$ is a constant diagonal matrix; (24) is substituted into (19) to obtain

$$\dot{S}_{PID} = \widetilde{f} - KS_{PID}, \tag{25}$$

where $\widetilde{f} = \hat{f} - f$.

Let us consider the following Lyapunov function candidate:

$$V = V_1 + V_2 + V_3, \tag{26}$$

where

$$V_1 = \frac{1}{2} \sum_{i=1}^{6} \left(\widetilde{W}_i^T \gamma_i^{-1} \widetilde{W}_i \right) \tag{27}$$

$$V_2 = \frac{1}{2} S_{PID}^T S_{PID} \tag{28}$$

$$V_3 = \frac{1}{2} \sum_{i=1}^{6} \widetilde{\Theta}_i^T \widetilde{\Theta}_i. \tag{29}$$

Lemma 2 [19]. *The time derivative of (26) has the following upper bound:*

$$\dot{V} \leq -\rho V + \mu, \tag{30}$$

where $\rho, \ \mu > 0$.

Proof. We differentiate (27) as follows:

$$\dot{V}_1 = \sum_{i=1}^{6} \widetilde{W}_i^T \gamma_i^{-1} \dot{\widetilde{W}}_i, \tag{31}$$

As W^* is a constant, and $\dot{\widetilde{W}} = \dot{\hat{W}}$, (31) becomes

$$\dot{V}_1 = \sum_{i=1}^{6} \widetilde{W}_i^T \gamma_i^{-1} \dot{\hat{W}}_i. \tag{32}$$

The update law can now be proposed as

$$\dot{\hat{W}}_i = -\gamma_i (S_{PIDi} \phi_i(S_{PIDi}) + \alpha_i \hat{W}_i), i = 1, 2, \ldots, 6, \tag{33}$$

where α_i is a small constant used to represent an amendment that helps improve the robustness of the control system.

By substituting the update law (33) into (32), $\dot{V}$ becomes

$$\dot{V}_1 = -\sum_{i=1}^{6} S_{PIDi} \widetilde{W}_i^T \phi_i(S_{PIDi}) - \sum_{i=1}^{6} \alpha_i \widetilde{W}_i^T \hat{W}_i, \tag{34}$$

where

$$-\widetilde{W}_i^T \hat{W}_i = -\widetilde{W}_i^T W_i^* - \widetilde{W}_i^T \widetilde{W}_i. \tag{35}$$

From (35), we obtain

$$-\frac{1}{2}\left(\widetilde{W}_i{}^T\widetilde{W}_i + W_i^{*T}W_i^*\right) \leq -\widetilde{W}_i{}^T W_i^* \leq \frac{1}{2}\left(\widetilde{W}_i{}^T\widetilde{W}_i + W_i^{*T}W_i^*\right). \tag{36}$$

Combining (36) with (35), we obtain

$$-\widetilde{W}_i{}^T\hat{W}_i \leq \frac{1}{2}\widetilde{W}_i{}^T\widetilde{W}_i + \frac{1}{2}W_i^{*T}W_i^* - \widetilde{W}_i{}^T\widetilde{W}_i \leq -\frac{1}{2}\widetilde{W}_i{}^T\widetilde{W}_i + \frac{1}{2}W_i^{*T}W_i^*. \tag{37}$$

From (37), the following inequality holds:

$$\dot{V}_1 \leq -\sum_{i=1}^{6} S_{PIDi}\widetilde{W}_i{}^T\boldsymbol{\phi}_i(S_{PIDi}) - \sum_{i=1}^{6}\frac{\alpha_i}{2}\widetilde{W}_i{}^T\widetilde{W}_i + \sum_{i=1}^{6}\frac{\alpha_i}{2}W_i^{*T}W_i^*. \tag{38}$$

We take the derivative of (28) to derive

$$\begin{aligned}\dot{V}_2 &= S_{PID}{}^T\dot{S}_{PID} \\ &= S_{PID}{}^T\left(\widetilde{f} - KS_{PID}\right)\end{aligned}. \tag{39}$$

Then, we invoke (20) and (23) to obtain

$$\begin{aligned}\dot{V}_2 &= \sum_{i=1}^{6} S_{PIDi}\left(\hat{W}_i^T\boldsymbol{\phi}_i(S_{PID}) - W_i^{*T}\boldsymbol{\phi}_i(S_{PID})\right) + S_{PID}{}^T(\boldsymbol{\varepsilon} - KS_{PID}) \\ &= \sum_{i=1}^{6} S_{PIDi}\widetilde{W}_i^T\boldsymbol{\phi}_i(S_{PID}) + S_{PID}{}^T\boldsymbol{\varepsilon} - S_{PID}{}^T KS_{PID}\end{aligned}. \tag{40}$$

Here, $\widetilde{W}^T = \hat{W}_i^T - W_i^{*T}$.

From (40), the PID sliding surface error can be obtained as follows:

$$S_{PID}{}^T\boldsymbol{\varepsilon} \leq \frac{1}{2}S_{PID}{}^T S_{PID} + \frac{1}{2}\boldsymbol{\varepsilon}^T\boldsymbol{\varepsilon}. \tag{41}$$

From (41), (40) yields the following inequality:

$$\dot{V}_2 \leq \sum_{i=1}^{6} S_{PIDi}\widetilde{W}^T\boldsymbol{\phi}_i(S_{PIDi}) + \frac{1}{2}S_{PID}{}^T S_{PID} + \frac{1}{2}\boldsymbol{\varepsilon}^T\boldsymbol{\varepsilon} - S_{PID}{}^T KS_{PID}. \tag{42}$$

The differential term of the PID sliding mode surface corresponds to the dynamic equation of AUVs (7), which can be divided into a standard term and an uncertainty term. Because AUVs exhibit high nonlinearity, high coupling, and strong interference, the dynamic equation of the standard term is inaccurate, and the PID sliding mode surface requires a high model accuracy; thus, an observer needs to be designed to compensate for the uncertainty term. From (14), we obtain

$$\dot{v} = \check{\tau} + \check{\tau}_{d\eta} - \check{C}(v)v - \check{D}(v)v - \check{g}(\eta), \tag{43}$$

where $\check{\tau} = \hat{M}^{-1}\tau$, $\check{C}(v) = \hat{M}^{-1}\hat{C}(v)$, $\check{D}(v) = \hat{M}^{-1}\hat{D}(v)$, $\check{g}(\eta) = \hat{M}^{-1}\hat{g}(\eta)$, $\check{\tau}_{d\eta} = \hat{M}^{-1}\tau_{d\eta}$.

As $\check{\tau}_{id\eta}$ of $\dot{v}_i$ in (43) is an unknown term, a high-order nonlinear observer π_i was designed, and the observer is referenced from [25]:

$$\begin{aligned}\dot{\pi}_{i0} &= \pi_{i1} - \check{C}_i(v_i)v_i - \check{D}_i(v_i)v_i - \check{g}_i(\eta_i) + \vartheta_{i0}(v_i - \pi_{i0}) \\ \dot{\pi}_{i1} &= \pi_{i2} + \vartheta_{i1}(v_i - \pi_{i0}) \\ \dot{\pi}_{i2} &= \pi_{i3} + \vartheta_{i2}(v_i - \pi_{i0}) \\ &\vdots \\ \dot{\pi}_{im} &= \vartheta_{im}(v_i - \pi_{i0}),\end{aligned} \tag{44}$$

where π_{i0}, π_{i1}, π_{i2}, $\ldots$, π_{im} is the estimated value of v_i, $\check{\tau}_{id\eta}$, $\dot{\check{\tau}}_{id\eta}$, $\ldots$, $\tau^{(m)}{}_{id\eta}$, and ϑ_{i0}, $\ldots$, $\vartheta_{im} > 0$. We obtain $\Theta_{i0}(t) = v_i - \pi_{i0}$, $\Theta_{i1}(t) = \check{\tau}_{id\eta} - \pi_{i1}$, $\ldots$, $\Theta_{im}(t) = \check{\tau}_{id\eta}^{(m)} - \pi_{im}$, and by combining it with (44), we obtain

$$
\begin{aligned}
\dot{\widetilde{\Theta}}_{i0} &= \widetilde{\Theta}_{i1} - \vartheta_{i0}\widetilde{\Theta}_{i0} \\
\dot{\widetilde{\Theta}}_{i1} &= \widetilde{\Theta}_{i2} - \vartheta_{i1}\widetilde{\Theta}_{i0} \\
\dot{\widetilde{\Theta}}_{i2} &= \widetilde{\Theta}_{i3} - \vartheta_{i2}\widetilde{\Theta}_{i0} \\
&\vdots \\
\dot{\widetilde{\Theta}}_{im} &= \check{\tau}_{id\eta}^{(m)} - \vartheta_{im}\widetilde{\Theta}_{i0}
\end{aligned}
\tag{45}
$$

Combining (44) and (45), we obtain

$$
\dot{\widetilde{\Theta}}_i = \boldsymbol{\varphi}_i\widetilde{\boldsymbol{\Theta}}_i + \boldsymbol{\Gamma}_i\check{\tau}_{id\eta}^{(m)},
\tag{46}
$$

where

$$
\boldsymbol{\varphi}_i = \begin{bmatrix}
-\vartheta_{i0} & 1 & 0 & \cdots & 0 \\
-\vartheta_{i1} & 1 & 1 & \cdots & 0 \\
\vdots & \vdots & \vdots & \ddots & \vdots \\
-\vartheta_{im-1} & 0 & 0 & \cdots & 1 \\
-\vartheta_{im} & 0 & 0 & \cdots & 0
\end{bmatrix}, \ \boldsymbol{\Gamma}_i = \begin{bmatrix}
0 \\
\vdots \\
\vdots \\
\vdots \\
1
\end{bmatrix}.
\tag{47}
$$

Then, we select a positive definite function (29):

$$
V_{3i} = \frac{1}{2}\widetilde{\boldsymbol{\Theta}}_i^T\widetilde{\boldsymbol{\Theta}}_i.
\tag{48}
$$

Differentiating V_{3i} and combining it with (46), we have

$$
\dot{V}_{3i} = \widetilde{\boldsymbol{\Theta}}_i^T\dot{\widetilde{\boldsymbol{\Theta}}}_i = \widetilde{\boldsymbol{\Theta}}_i^T\left(\boldsymbol{\varphi}_i\widetilde{\boldsymbol{\Theta}}_i + \boldsymbol{\Gamma}_i\check{\tau}_{id\eta}^{(m)}\right).
\tag{49}
$$

Combining (49) and the result of lemma 1, we obtain

$$
\dot{V}_{3i} \le \widetilde{\boldsymbol{\Theta}}_i^T(\boldsymbol{\varphi}_i + \delta_i\boldsymbol{I})\widetilde{\boldsymbol{\Theta}}_i + \frac{1}{\delta_i}\sigma_i^2,
\tag{50}
$$

where $\delta_i > 0$, $i = 1, 2, \ldots, 6$, σ_i^2 is the quadratic square of $\check{\tau}_{id\eta}^{(m)}$.

Now, we can differentiate V_3 as follows:

$$
\dot{V}_3 = \sum_{i=1}^{6}\widetilde{\boldsymbol{\Theta}}_i^T\dot{\widetilde{\boldsymbol{\Theta}}}_i.
\tag{51}
$$

Substituting (50) into (51), we obtain

$$
\dot{V}_3 \le \sum_{i=1}^{6}\widetilde{\boldsymbol{\Theta}}_i^T(\boldsymbol{\varphi}_i + \delta_i\boldsymbol{I})\widetilde{\boldsymbol{\Theta}}_i + \frac{1}{\delta_i}\sigma_i^2.
\tag{52}
$$

Differentiating (26) and combining (38), (42), and (52), we obtain

$$\dot{V} = \dot{V}_1 + \dot{V}_2 + \dot{V}_3$$
$$\leq -\sum_{i=1}^{6} S_{PIDi} \widetilde{W}_i^T \boldsymbol{\phi}_i(S_{PIDi}) - \sum_{i=1}^{6} \frac{\alpha_i}{2} \widetilde{W}_i^T \widetilde{W}_i + \sum_{i=1}^{6} \frac{\alpha_i}{2} W_i^{*T} W_i^* +$$
$$\sum_{i=1}^{6} S_{PIDi} \widetilde{W}^T \phi_i(S_{PID}) + \frac{1}{2} S_{PID}^T S_{PID} + \frac{1}{2} \boldsymbol{\varepsilon}^T \boldsymbol{\varepsilon} - S_{PID}^T K S_{PID} + \sum_{i=1}^{6} \widetilde{\Theta}_i^T (\boldsymbol{\varphi}_i + \delta_i I) \widetilde{\Theta}_i +$$
$$\sum_{i=1}^{6} \frac{1}{\delta_i} \sigma_i^2$$
$$\leq -S_{PID}^T \left(K - \frac{1}{2} I \right) S_{PID} - \sum_{i=1}^{6} \frac{\alpha_i}{2} \widetilde{W}_i^T \widetilde{W}_i - \sum_{i=1}^{6} \widetilde{\Theta}_i^T (-\boldsymbol{\varphi}_i - \delta_i I) \widetilde{\Theta}_i + \sum_{i=1}^{6} \frac{1}{\delta_i} \sigma_i^2 +$$
$$\sum_{i=1}^{6} \frac{\alpha_i}{2} W_i^{*T} W_i^* + \frac{1}{2} \boldsymbol{\varepsilon}^T \boldsymbol{\varepsilon}$$
(53)

Then, citing lemma 2, we obtain

$$\dot{V} \leq -\rho(V_1 + V_2 + V_3) + \mu, \tag{54}$$

where

$$\rho = min\left(\min_{i=1,\,2,\ldots,6}(\alpha_i),\ 2\lambda_{min}\left(K - \frac{1}{2}I \right), -2\lambda_{min}(\boldsymbol{\varphi}_i + \delta_i I) \right) \tag{55}$$

$$\mu = \sum_{i=1}^{6} \frac{1}{\delta_i} \sigma_i^2 + \sum_{i=1}^{6} \frac{\alpha_i}{2} W_i^{*T} W_i^* + \frac{1}{2} \boldsymbol{\varepsilon}^T \boldsymbol{\varepsilon}. \tag{56}$$

The variable $\lambda_{min}(\cdot)$ represents the minimum eigenvalue of the matrix. We assume $\lambda_{min}\left(K - \frac{1}{2}I \right) > 0$ and $\lambda_{min}(\boldsymbol{\varphi}_i + \delta_i I) < 0$ to ensure that $\rho > 0$. The variable μ is a scalar and $\mu > 0$.

Thus, the proof is complete.

Theorem 1. *For the AUV system described in (7), under the control law (24) and the update law (33), as long as the initial conditions are bounded, the sliding surface errors and their derivatives are semi-globally uniformly bounded.*

Proof. Multiplying (54) with $e^{\rho t}$, we obtain

$$\frac{d}{dt}\left(V e^{\rho t} \right) \leq \mu e^{\rho t}. \tag{57}$$

Integrating (57), we obtain

$$V \leq \frac{\mu}{\rho} + e^{-\rho t}\left(V(0) - \frac{\mu}{\rho} \right) \leq \frac{\mu}{\rho} + V(0)e^{-\rho t}. \tag{58}$$

Substituting (27), (28), and (29) separately into (58), we obtain

$$V_1 = \frac{1}{2} \sum_{i=1}^{6} \left(\widetilde{W}_i^T \gamma_i^{-1} \widetilde{W}_i \right) \leq V \leq \frac{\mu}{\rho} + V(0)e^{-\rho t} \tag{59}$$

$$V_2 = \frac{1}{2} S_{PID}^T S_{PID} \leq V \leq \frac{\mu}{\rho} + V(0)e^{-\rho t} \tag{60}$$

$$V_3 = \frac{1}{2} \sum_{i=1}^{6} \widetilde{\Theta}_i^T \widetilde{\Theta}_i \leq V \leq \frac{\mu}{\rho} + V(0)e^{-\rho t} \tag{61}$$

$$\Omega \widetilde{W}_i := \left\{ \widetilde{W}_i \in R^6 \,\middle|\, \| \widetilde{W}_i \| \leq \sqrt{2} \sqrt{\frac{\left(\frac{\mu}{\rho} + V(0)e^{-\rho t} \right)}{\min_{i=1,\,2,\ldots,6}(\gamma_i^{-1})}} \right\},\ i = 1,\ldots,6 \quad \forall t \in [0,+\infty)$$
(62)

$$\Omega S_{PID} := \left\{ S_{PID} \in R^6 \,\middle|\, \| S_{PID} \| \leq \sqrt{2} \sqrt{\frac{\mu}{\rho} + V(0)e^{-\rho t}} \right\} \forall t \in [0,+\infty) \tag{63}$$

$$\Omega\widetilde{\boldsymbol{\Theta}}_i := \left\{ \widetilde{\boldsymbol{\Theta}}_i \in R^6 \,\middle|\, \| \widetilde{\boldsymbol{\Theta}}_i \| \le \sqrt{2}\sqrt{\frac{\mu}{\rho} + V(0)e^{-\rho t}} \right\}, \ i = 1,\dots,6 \ \ \forall t \in [0,+\infty). \quad (64)$$

Thus, the proof is complete.

Based on Theorem 2, we can verify that S_{PID} can reach the neighborhood of zero in a finite time t_{reach}; thus, we obtain

$$
\begin{aligned}
\boldsymbol{K}_P \boldsymbol{S}_{\widetilde{v}} + \boldsymbol{K}_I \int_0^t \boldsymbol{S}_{\widetilde{v}} dt + \boldsymbol{K}_D \frac{d\boldsymbol{S}_{\widetilde{v}}}{dt} &= 0 \\
K_{Pi} S_{\widetilde{v}i} + K_{Ii} \int_0^t S_{\widetilde{v}i} dt + K_{Di} \frac{dS_{\widetilde{v}i}}{dt} &= 0, \ i = 1, \dots, 6.
\end{aligned}
\quad (65)
$$

As long as $K_{Pi}^2 - 4K_{Ii}K_{Di} \ge 0$, $i = 1, \dots, 6$, is satisfied; the second-order differential equation for (65) can be expressed as

$$\int_0^t S_{\widetilde{v}i} dt = C_1 e^{\frac{-K_{Pi}+\sqrt{K_{Pi}^2-4K_{Ii}K_{Di}}}{2K_{Di}}t} + C_2 e^{\frac{-K_{Pi}-\sqrt{K_{Pi}^2-4K_{Ii}K_{Di}}}{2K_{Di}}t}. \quad (66)$$

From (66), $\int_0^t S_{\widetilde{v}i} dt$ can have a time limit of t_{ci} exponent converging to the neighborhood of zero, which proves that $S_{\widetilde{v}i}$ can also be a finite-time t_{ci} exponent, converging to the neighborhood of zero.

From the above analysis, we have a speed-tracking error that converges to the neighborhood of zero in limited time, and the total time spent to converge to the neighborhood of zero is initially $S_{\widetilde{v}}(0)$; thus, the total time can be expressed as

$$t_{sum} = t_{reach} + \max_{i = 1,2,\dots,6}(t_c). \quad (67)$$

At $t > t_{sum}$, we obtain the following from (13):

$$\boldsymbol{v} = \boldsymbol{v}_c. \quad (68)$$

We can obtain the region where $S_{\widetilde{v}}$ can converge to the neighborhood of zero from (68) and, by substituting it into (13), we obtain

$$
\begin{aligned}
\dot{\widetilde{\boldsymbol{\eta}}} + \boldsymbol{K}_1 \widetilde{\boldsymbol{\eta}} + \boldsymbol{K}_2 \int_0^t \widetilde{\boldsymbol{\eta}} dt &= 0 \\
\dot{\widetilde{\eta}}_i + K_{1i} \widetilde{\eta}_i + K_{2i} \int_0^t \widetilde{\eta}_i dt &= 0, i = 1, \dots, 6
\end{aligned}
\quad (69)
$$

As long as $K_{1i}^2 - 4K_{2i} \ge 0$, $\int_0^t \widetilde{\eta}_i dt$ $(i = 1, \dots, 6)$ is satisfied, $\widetilde{\boldsymbol{\eta}}$ can converge to the neighborhood of zero in limited time. Therefore, similar to the speed-tracking error of (66), the position-tracking error will also converge to the neighborhood of zero exponentially after t_{sum}.

Remark 1. *Equation (69) can be regarded as a second-order system with zero input, and its natural frequency and damping ratio can be expressed as $\omega_n = \sqrt{\frac{K_2}{1}}$ and $\zeta = \frac{K_1}{2\sqrt{K_2 * 1}}$, respectively. By using the time-domain method, we assume $K_{1i}^2 - 4K_{2i} \ge 0$, $i = 1, \dots, 6$. The system can converge exponentially. When the damping ratio ζ is closer to 0.707, the convergence speed of the second-order system is relatively fast, while the overshoot is relatively small, which is the state with the best comprehensive performance of the second-order system.*

4. Simulation Results

Because the AUV dynamic model is complex and unstable under uncertain conditions and ocean current disturbances, the simulation control of AUV motion behavior is challenging. This paper verified the effectiveness of this method by using the new AUV model, presented in Figure 4, to conduct a Gazebo visual real-time simulation. This is a fully actuated AUV, which is driven with six degrees of freedom through the configuration of eight propeller groups, as shown in Figure 4. This is a universal model and thus can be used to verify the superiority of various control methods. Its parameters are listed in Table 1.
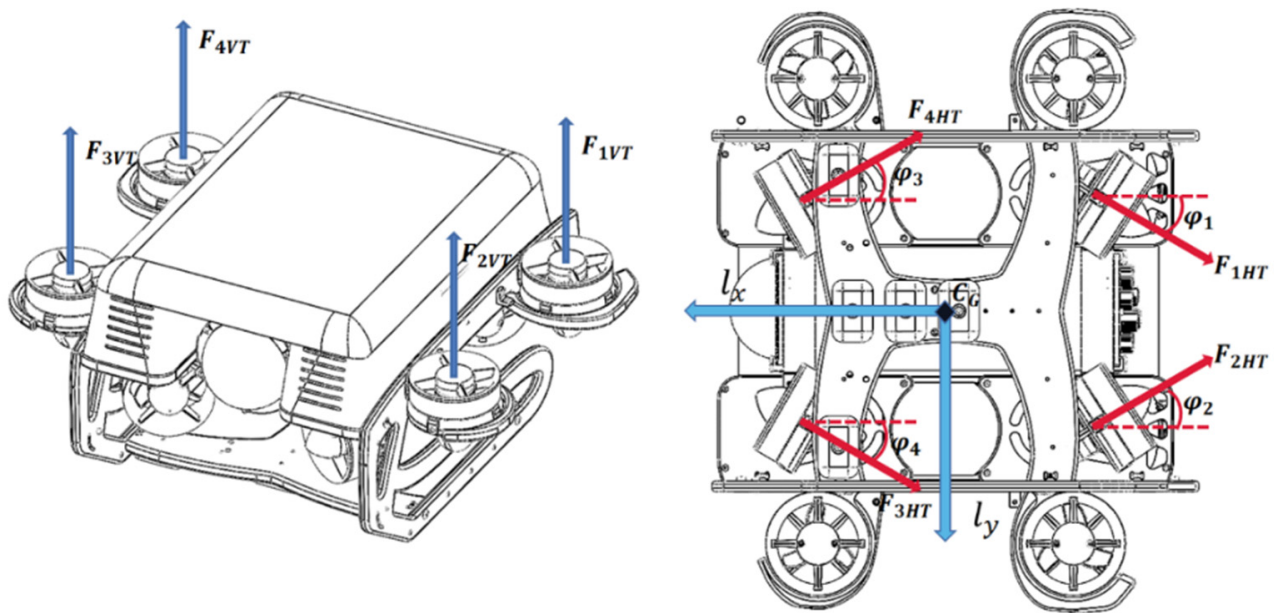

Figure 4. Structure and thruster distribution of an AUV.

Gazebo comprises an AUV simulator, which is a functional package developed under the robot operating system (ROS) and has the function of simulating a real underwater environment. We added ocean current interference to the underwater environment to make it more realistic. Dave is a derivative plug-in developed based on the AUV simulator, which can simulate the effects of underwater ocean currents.

As shown in Figure 5, the 3D model of an AUV was imported into the Gazebo underwater simulation environment. In this environment, the trajectory-tracking control simulation could easily verify whether the control system operated as expected. The proposed control method was compared with the methods of RBF neural network PID sliding mode control (RBFPIDSMC) and RBF neural network PD sliding mode control (RBFPDSMC) proposed in [29] and [32], respectively. The three control methods operated in the same initial conditions and the same external disturbance in the two trajectory-tracking control simulations. Moreover, all three methods selected a group of well-performing parameters through Lyapunov stability theory and multiple simulations. The controller parameters used in this paper are shown in Table 2.

Table 1. Control parameters used in the simulation.

| Parameters	Units	Value	Description
$X_{\dot{u}}$	kg	−5.5	Added mass
X_u	kg/s	−4.03	Linear damping
$X_{u\|u\|}$	kg/m	−18.18	Axial drag
$Y_{\dot{v}}$	kg	−12.7	Added mass
$Y_{\dot{r}}$	kg m	1.93	Added mass
Y_v	kg/s	−6.22	Linear damping
$Y_{v\|v\|}$	kg/m	−21.66	Axial drag
$Z_{\dot{w}}$	kg	−14.57	Added mass
$Z_{\dot{q}}$	kg m	−1.7	Added mass
Z_w	kg/s	−5.18	Linear damping
$Z_{w\|w\|}$	kg/m	−36.99	Axial drag
$K_{\dot{p}}$	kg m	−0.12	Added mass
K_p	kg m/s	−0.07	Linear damping
$K_{p\|p\|}$	kg m	−1.55	Crossflow drag
$M_{\dot{q}}$	kg m	−0.12	Added mass
$M_{\dot{w}}$	Kg	−0.04	Added mass
M_q	kg m/s	−0.07	Linear damping
$M_{q\|q\|}$	kg m	−1.55	Crossflow drag
$N_{\dot{r}}$	kg m	−0.12	Added mass
$N_{\dot{v}}$	kg	0.04	Added mass
N_r	kg m/s	−0.07	Linear damping
$N_{r\|r\|}$	kg m	−1.55	Crossflow drag
m	kg	11.5	Center of gravity
I_{xx}	kg m^2	0.099	Inertia tensor on the x-axis
I_{yy}	kg m^2	0.129	Inertia tensor on the y-axis
I_{zz}	kg m^2	0.16	Inertia tensor on the z-axis
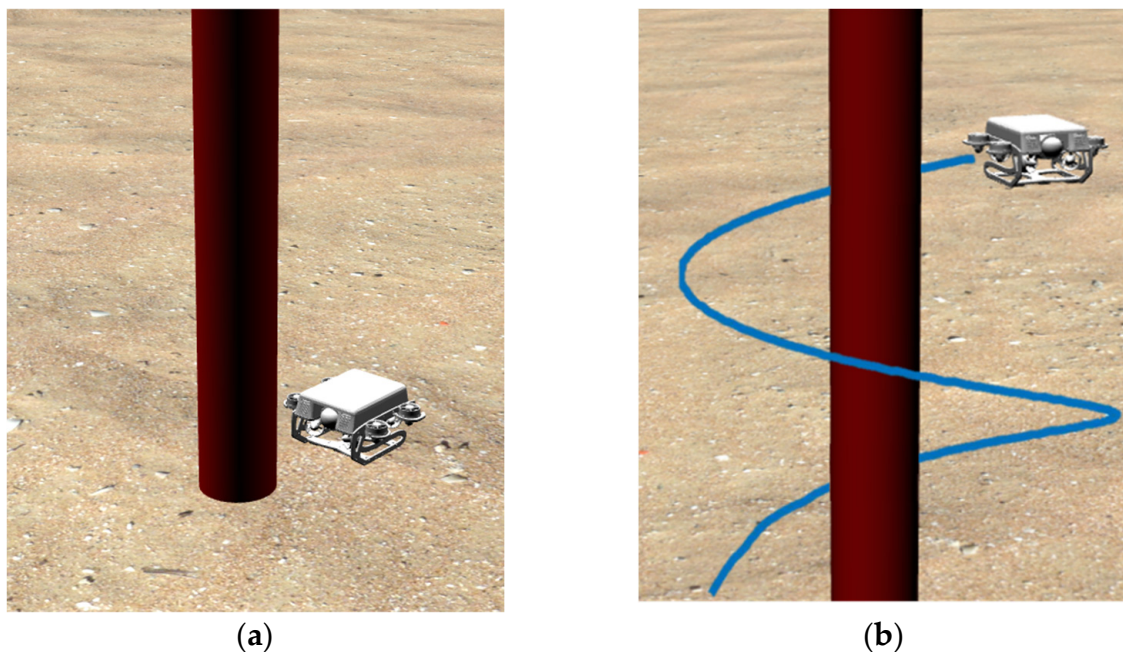
Figure 5. AUV in a simulated underwater environment. (**a**) Hover; (**b**) motion trail.

Table 2. Control parameters used in the simulations.

Controller	Parameters
RBFPDSMC	$K_p = \text{diag}[0.0035, 0.0014, 0.0016, 0.004, 0.0048, 0.0025]$, $K_D = \text{diag}[0.3, 0.15, 0.15, 0.07, 0.07, 0.08]$ $K = \text{diag}[0.1, 0.1, 0.1, 0.1, 0.1, 0.1]$
RBFPIDSMC	$K_p = \text{diag}[0.0045, 0.0017, 0.002, 0.005, 0.0068, 0.0015]$, $K_I = \text{diag}[0.00012, 0.00012, 0.00012, 0.0001, 0.0001, 0.00012]$ $K_D = \text{diag}[0.2, 0.13, 0.218, 0.07, 0.06, 0.1]$ $\kappa = \text{diag}[0.1, 0.1, 0.1, 0.1, 0.1, 0.1]$, $\eta = \text{diag}[0.2, 0.2, 0.2, 0.05, 0.05, 0.05]$
DLNNSMC	$\gamma = [0.37, 0.35, 0.45, 25, 25, 32]$, $\alpha = [0.005, 0.005, 0.005, 0.005, 0.005, 0.0035]$, $K = \text{diag}[0.3, 0.3, 0.3, 0.3, 0.3, 0.3]$, $K_1 = \text{diag}[1.05, 1, 0.5, 1, 1, 2.1]$, $K_2 = \text{diag}[0.01, 0.01, 0.01, 0.01, 0.01, 0.01]$, $K_p = \text{diag}[0.05, 0.05, 0.07, 0.05, 0.03, 0.084]$, $K_I = \text{diag}[0.0001, 0.0001, 0.0001, 0.0001, 0.0001, 0.0001]$, $K_D = \text{diag}[4.4, 4.4, 4.4, 0.5, 0.5, 0.3]$, $\vartheta_0 = [0.00038, 0.0008, 0.0008, 1, 1, 1]$, $\vartheta_1 = [0.21, 0.5, 0.6, 0.3, 0.4, 0.08]$, $\vartheta_2 = [0.00021, 0.0004, 0.0006]$

The RBFNN parameters of the three control methods were the same: $c_{ik} = [-0.2 - 0.1\ 0\ 0.1\ 0.2]$ and $b_{ik} = 5$.

4.1. Helix Track Tracking Control

First, the effectiveness and superiority of the control law were verified by tracking a spatial helical reference track. The tracked spirals are expressed as

$$\begin{cases} x_d(t) = sin(0.025t) + 25.1 \text{ m} \\ y_d(t) = cos(0.025t) - 1.05 \text{ m} \\ z_d(t) = 0.0184t - 93.7 \text{ m} \end{cases} \tag{70}$$

The initial motion state of AUVs can be expressed as $u_0 = 0(m/s)$, $v_0 = 0(m/s)$, $w_0 = 0(m/s)$, $p_0 = 0(rad/s)$, and $q_0 = 0(rad/s)$, where r_0 is a random variable, and the initial position and angle are $x = 25(m)$, $y = 0(m)$, $z = -94.8(m)$ and $\varphi = 0(rad)$, $\Theta = 0(rad)$, $\psi = 2.4(rad)$, respectively. Because the Dave plug-in can simulate the effect of ocean currents, the current in this experiment was considered a high-frequency random current in all directions: $V_c = rand(0 \sim 0.1 \text{ m/s})$, $\beta_c = rand(-1.57 \sim 1.57rad)$, $\alpha_c = rand(-1.57 \sim 1.57rad)$, where V_c is the current velocity, β_c is the sideslip angle, and α_c is the angle of attack. Thus, the linear velocity of the ocean current on the three axes of the EF frame can be defined as

$$\begin{cases} v_x = V_c cos\alpha cos\beta \\ v_y = V_c sin\beta \\ v_z = V_c sin\alpha cos\beta \end{cases} \tag{71}$$

Figure 6 shows a 3D view of AUV position tracking using these three control methods. All three methods could successfully make the underwater robot track the target trajectory. DLNNSMC yielded the best result. According to Section 3, $\widetilde{\eta} \in R^6$ is the position error vector, where $\widetilde{\eta}_1$, $\widetilde{\eta}_2$, and $\widetilde{\eta}_3$ are the position errors of the x-axis, y-axis, and z-axis of the EF frame, respectively. Now, we define the Euclidean distance of the position tracking error $D_E = \sqrt{\widetilde{\eta}_1^2 + \widetilde{\eta}_2^2 + \widetilde{\eta}_3^2}$; the average values of D_E for the three methods are listed in Table 3.
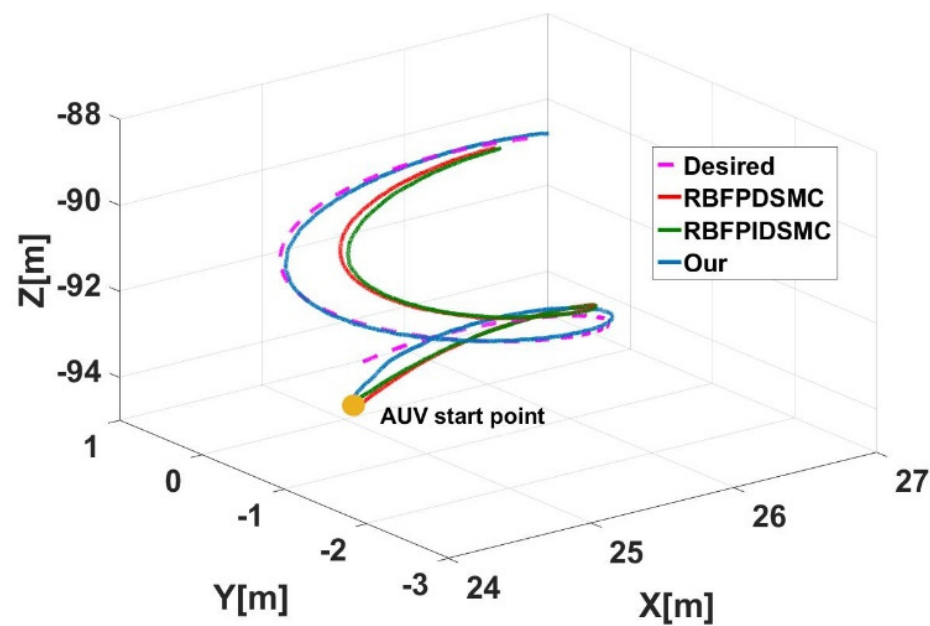
Figure 6. Three−dimensional view of the trajectory.

Table 3. Average values of D_E .

RBFPDSMC	RBFPIDSMC	DLNNSMC
0.442594	0.472352	0.116747

Table 3 shows that the average value of D_E for DLNNSMC was approximately 73.6% and 75.3% lower than that of RBFPDSMC and RBFPIDSMC, respectively.

Figure 7 shows the position tracking errors of six degrees of freedom: x_e, y_e, z_e, φ_e, Θ_e, and ψ_e. We analyzed the position tracking error and found that (1) The results obtained for all three methods indicated that the six degrees of freedom converged in a bounded region, while DLNNSMC could maintain a smaller range and a more stable bounded region; (2) In the degree of freedom with a large position tracking error (z-axis direction motion and yaw angle), the convergence time for the position tracking error on the z-axis was 150 s, while those for RBFPDSMC and RBFPIDSMC were both beyond 250 s. The convergence time for the yaw angle was 50 s, while RBFPDSMC and RBFPIDSMC could not achieve a complete convergence within 300 s. This showed that DLNNSMC had a faster convergence speed of position-tracking error.

Figure 8 shows the speed-tracking errors of six degrees of freedom: u_e, v_e, w_e, p_e, q_e, and r_e. We analyzed the velocity tracking error and found that (1) The velocity tracking errors of the three methods could converge to a certain range of bounded regions. Although the velocity tracking errors of the three Euler angles of DLNNSMC fluctuated considerably in the beginning, they could converge to a stable range in 100 s, and the velocity tracking errors in the three directions of motion evidently converged to a smaller range of bounded regions than with RBFPDSMC and RBFPIDSMC. (2) The convergence time of the velocity tracking error for DLNNSMC in the x-and z-axis directions was 50 s; RBFPDSMC and RBFPIDSMC could not achieve convergence on the x-axis, while the convergence time on the z-axis was 100 s. This indicated that DLNNSMC converged faster and more stably as regards the speed-tracking error.
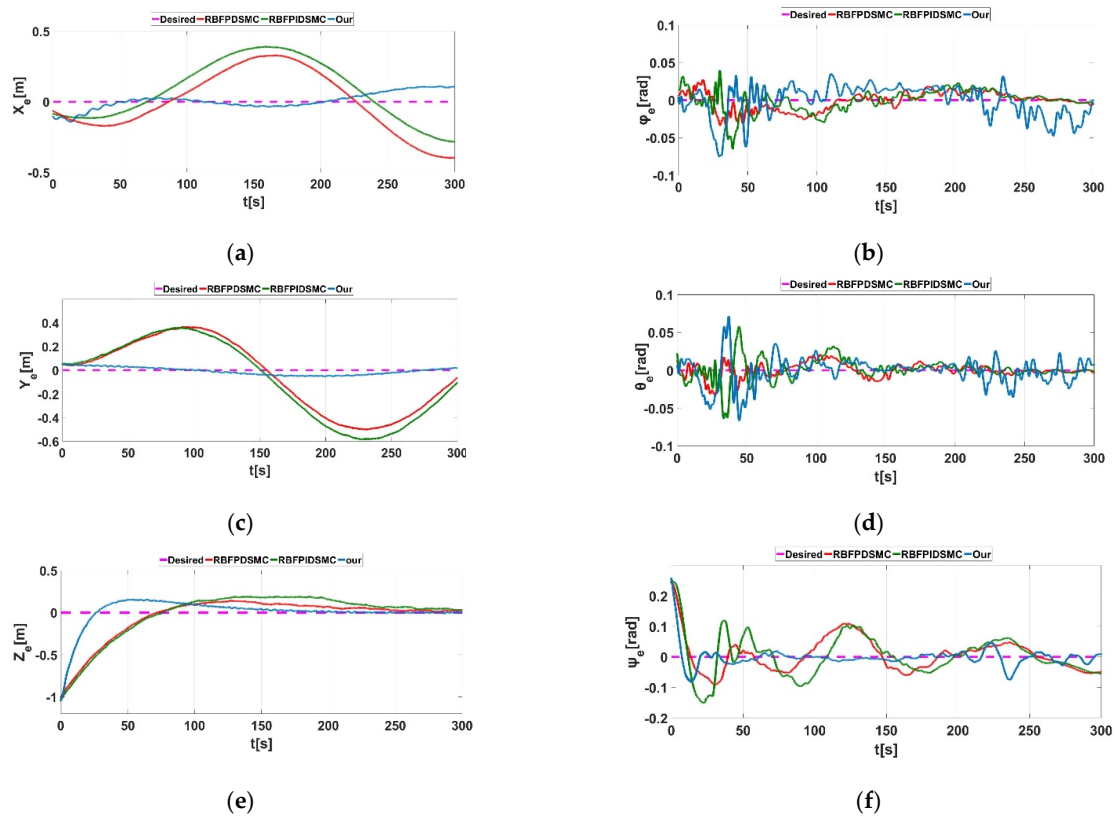
Figure 7. AUV position−tracking errors. (**a**) x_e; (**b**) φ_e; (**c**) y_e; (**d**) Θ_e; (**e**) z_e; (**f**) ψ_e.
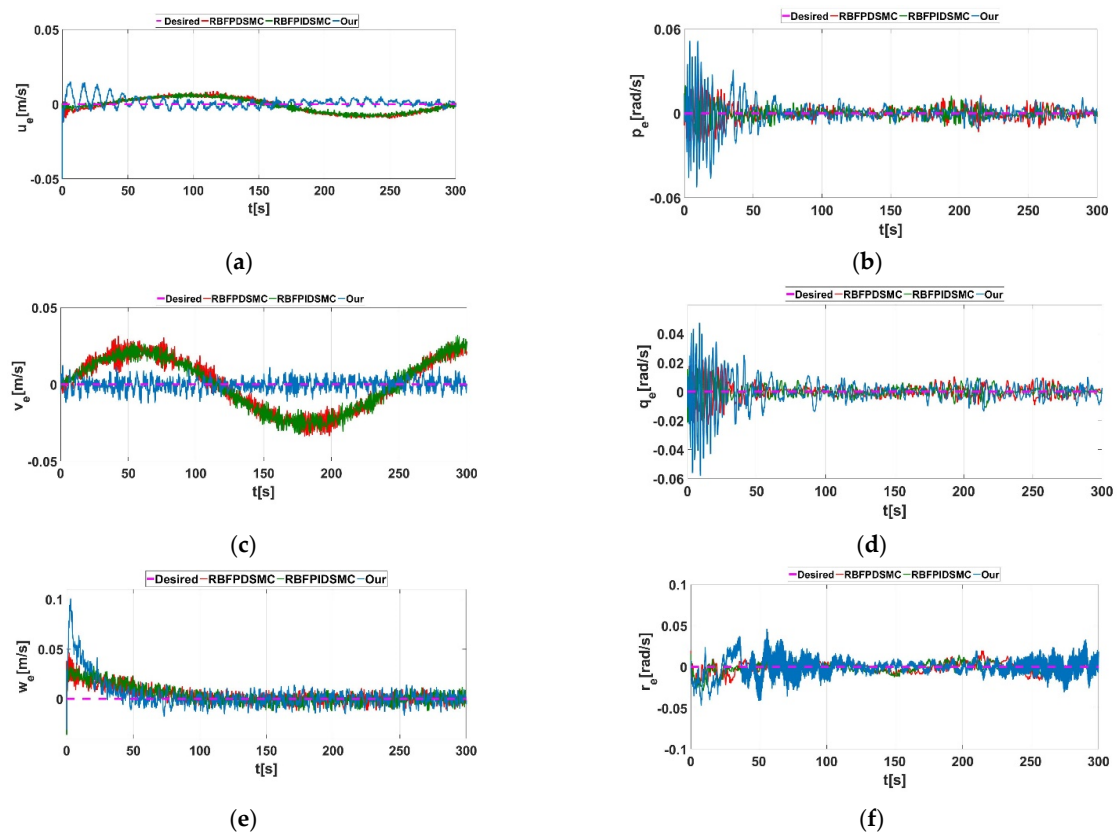
Figure 8. AUV velocity−tracking errors. (**a**) u_e; (**b**) p_e; (**c**) v_e; (**d**) q_e; (**e**) w_e; (**f**) r_e.

Figure 9 shows the change in the inner-loop PID sliding mode surface S_{PID} of DLNNSMC. S_{PID} continued to converge within a limited area. When the inner loop approached zero, the outer-loop PID sliding mode surface $S_{\tilde{v}}$ converged to the neighborhood of zero as an exponential function, as shown in Figure 10.
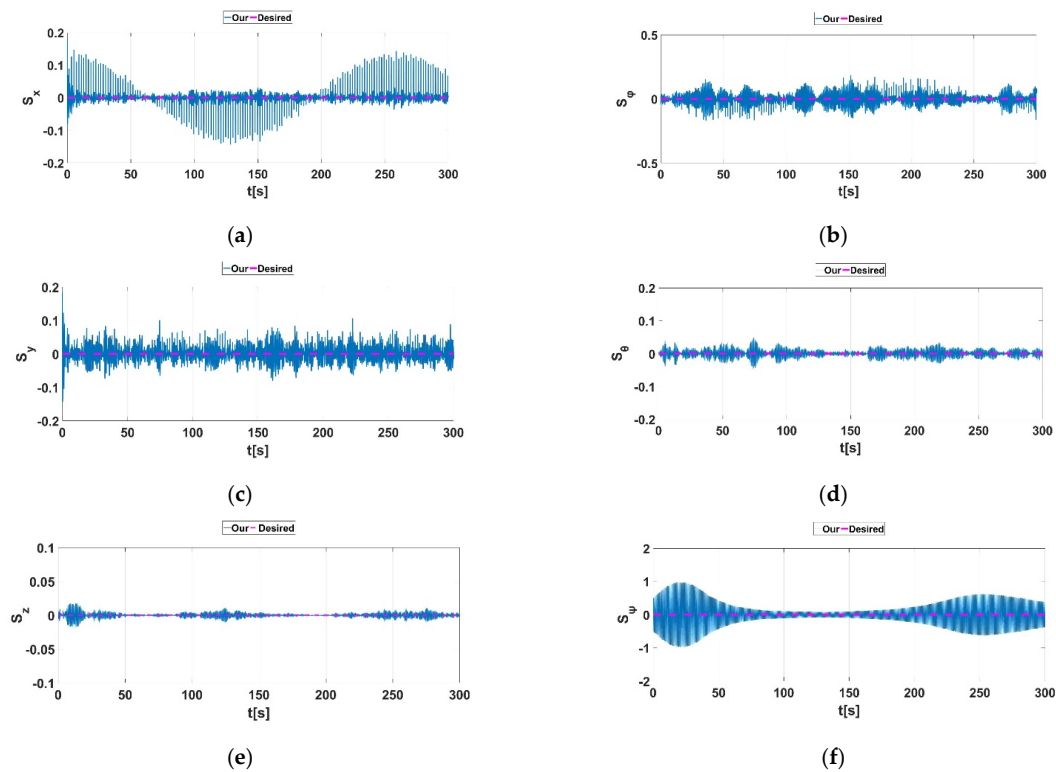

Figure 9. Inner−loop PID sliding surface S_{PID}. (**a**) S_x; (**b**) S_{φ}; (**c**) S_y; (**d**) S_{Θ}; (**e**) S_z; (**f**) S_{ψ}.
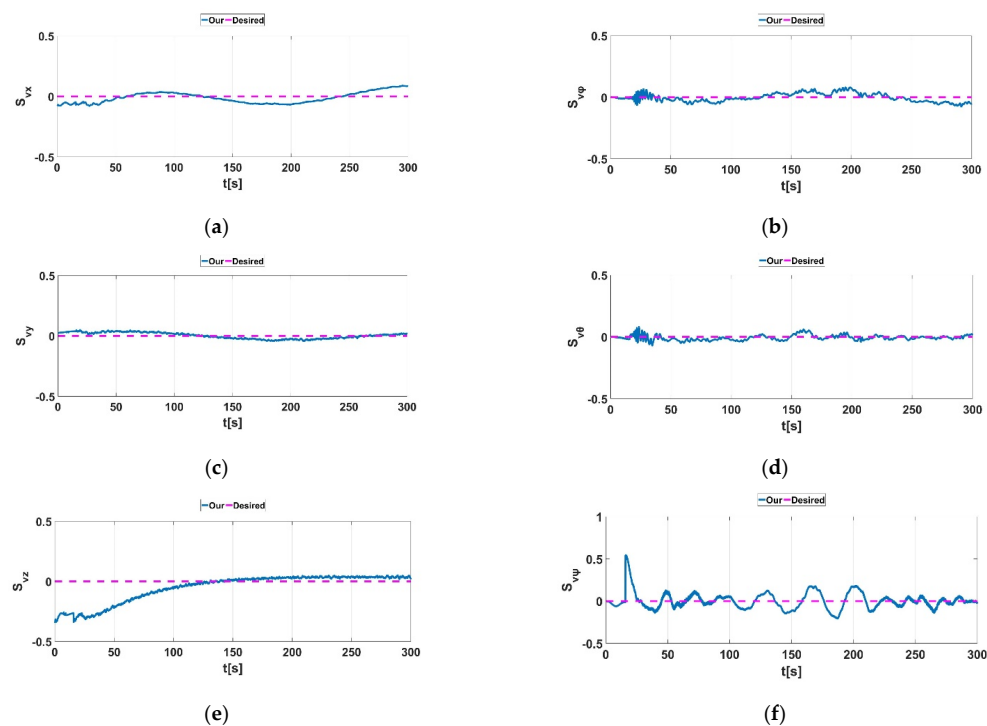
Figure 10. Outer−loop PID sliding surface $S_{\tilde{v}}$. (**a**) S_{vx}; (**b**) $S_{v\varphi}$; (**c**) S_{vy}; (**d**) $S_{v\Theta}$; (**e**) S_{vz}; (**f**) $S_{v\psi}$.

In the initial state of AUVs, the position error of the *z*-axis was 1 m, and the error of the yaw angle ψ was 0.24 rad. Figure 10 shows that $S_{\tilde{v}}$ gradually converged to the neighborhood of zero. From (69), we concluded that the position- and velocity-tracking errors of AUVs can converge to the neighborhood of zero.

4.2. Sinusoidal Trajectory Tracking Control

Second, the effectiveness and superiority of the control law were tested by tracking a spatial sinusoidal reference trajectory. The tracked sine line can be expressed as follows:

$$\begin{cases} x_d(t) = 0.0184t + 26 \text{ m} \\ y_d(t) = sin(0.025t) - 0.3 \text{ m} \\ z_d(t) = 0.0167t - 93.7 \text{ m} \\ \psi_d(t) = 0.1 * sin(0.025t) \text{ rad} \end{cases} . \tag{72}$$

Figure 11 shows a 3D view of AUV position tracking using the three control methods. Figures 12 and 13 show the tracking effect of the corresponding position- and speed-tracking errors, respectively. According to the tracking results shown in these figures, even if the yaw angle ψ also had angle tracking, the proposed DLNNSMC could still effectively track the required trajectory, had a faster convergence speed and higher tracking accuracy, and was stable in a smaller limited area. For DLNNSMC, the convergence times of position and velocity tracking errors were, approximately, 100 and 50 s, respectively. However, RBFPDSMC and RBFPIDSMC could not achieve an accurate convergence in six degrees of freedom at the same time. The average values of D_E for the three methods are listed in Table 4.
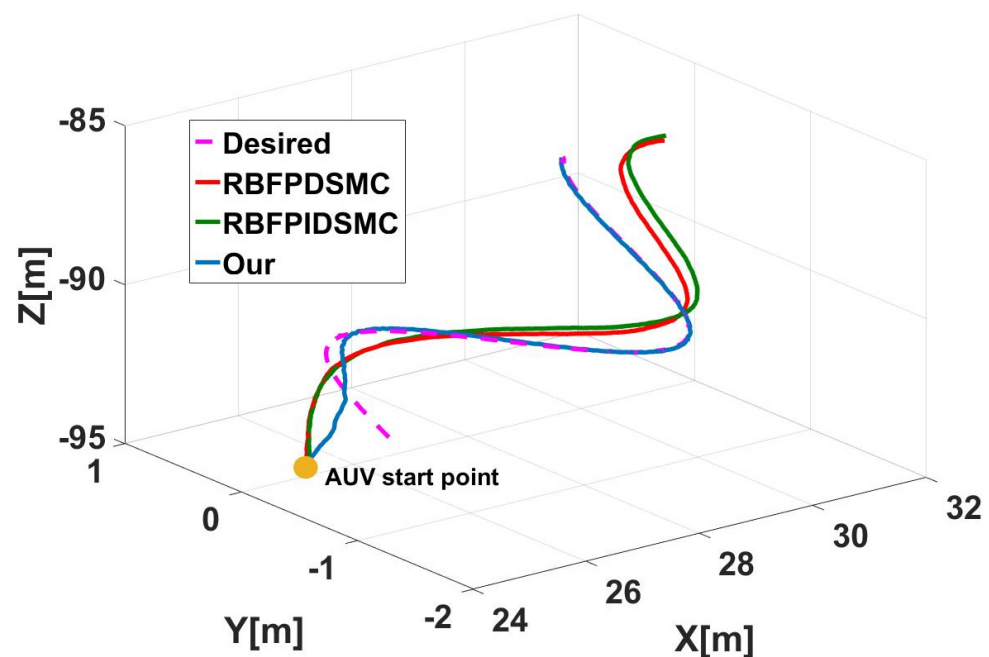

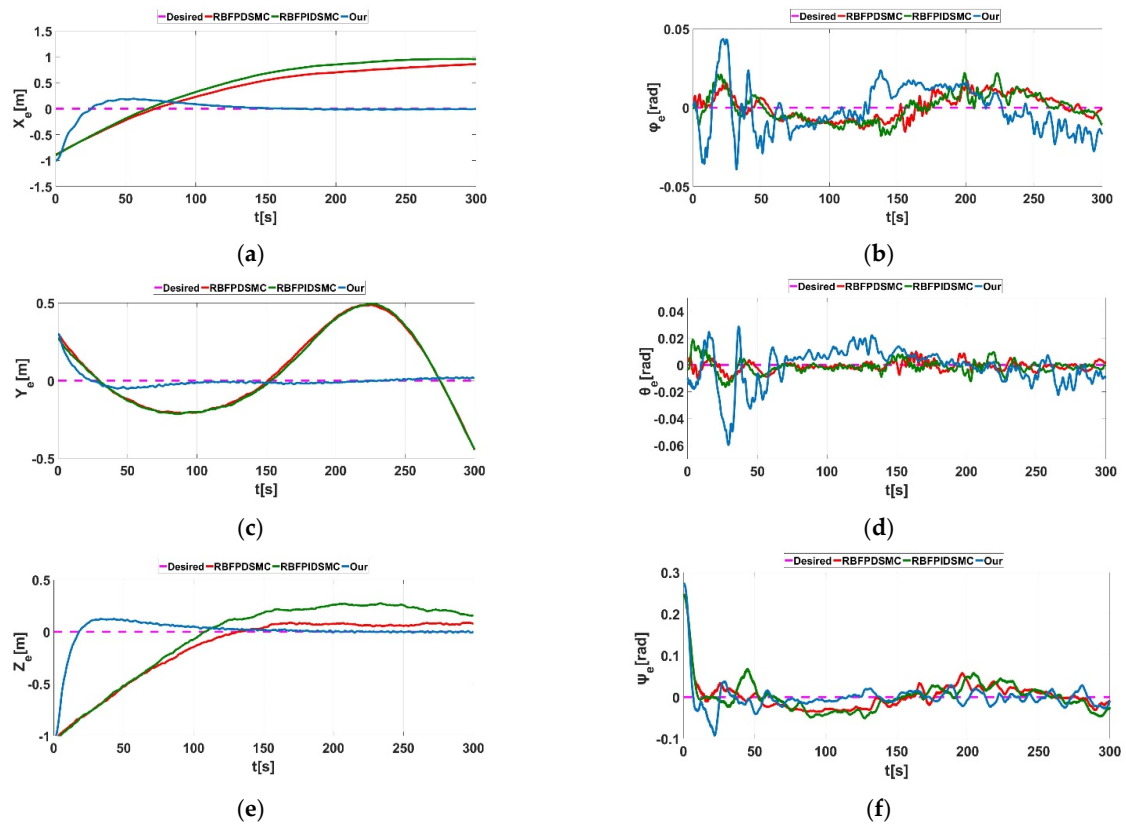**Figure 11.** Three−dimensional view of the trajectory.

Figure 12. AUV position−tracking errors. (**a**) x_e; (**b**) φ_e; (**c**) y_e; (**d**) Θ_e; (**e**) z_e; (**f**) ψ_e.
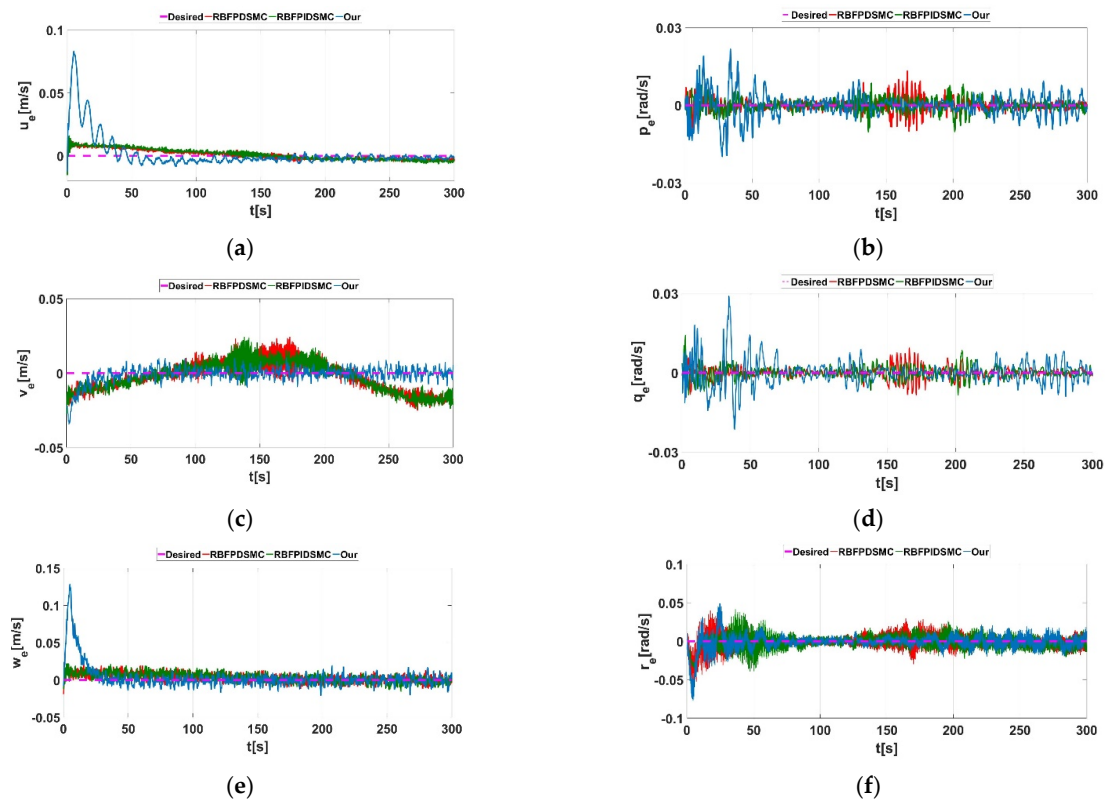
Figure 13. AUV velocity−tracking errors. (**a**) u_e; (**b**) p_e; (**c**) v_e; (**d**) q_e; (**e**) w_e; (**f**) r_e.

Table 4. Average values of D_E .

RBFPDSMC	RBFPIDSMC	DLNNSMC
0.804427	0.949559	0.105999

　　　　The initial motion state of AUVs can be expressed as $u_0 = 0 \ (m/s), v_0 = 0 \ (m/s)$, $w_0 = 0 \ (m/s)$ and $p_0 = 0 \ (rad/s), q_0 = 0 \ (rad/s)$; r_0 is a random variable, and the initial position and angle are $x = 25 \ (m), y = 0 \ (m), z = -94.8 \ (m)$ and $\varphi = 0 \ (rad)$, $\Theta = 0 \ (rad), \psi = 2.4 \ (rad)$, respectively. The current in this experiment was a high-frequency random current in all directions: $V_c = rand(0\text{–}0.1 \ \text{m/s}), \beta_c = rand(-1.57\text{–}1.57rad)$, $\alpha_c = rand(-1.57\text{–}1.57rad)$.

　　　　Table 4 shows that the average value of D_E for DLNNSMC was approximately 86.8% and 88.8% lower than that for RBFPDSMC and RBFPIDSMC, respectively.

　　　　Figure 14 shows the change in the inner-loop PID sliding mode surface $\boldsymbol{S}_{PID}$ of DLNNSMC. $\boldsymbol{S}_{PID}$ continued to converge in a limited region. Figure 15 shows the outer-loop PID sliding surface $\boldsymbol{S}_{\widetilde{v}}$, which could gradually converge exponentially to the neighborhood of zero even if it had a larger error. From (69), we concluded that the position-and speed-tracking errors of AUVs can converge to the neighborhood of zero.
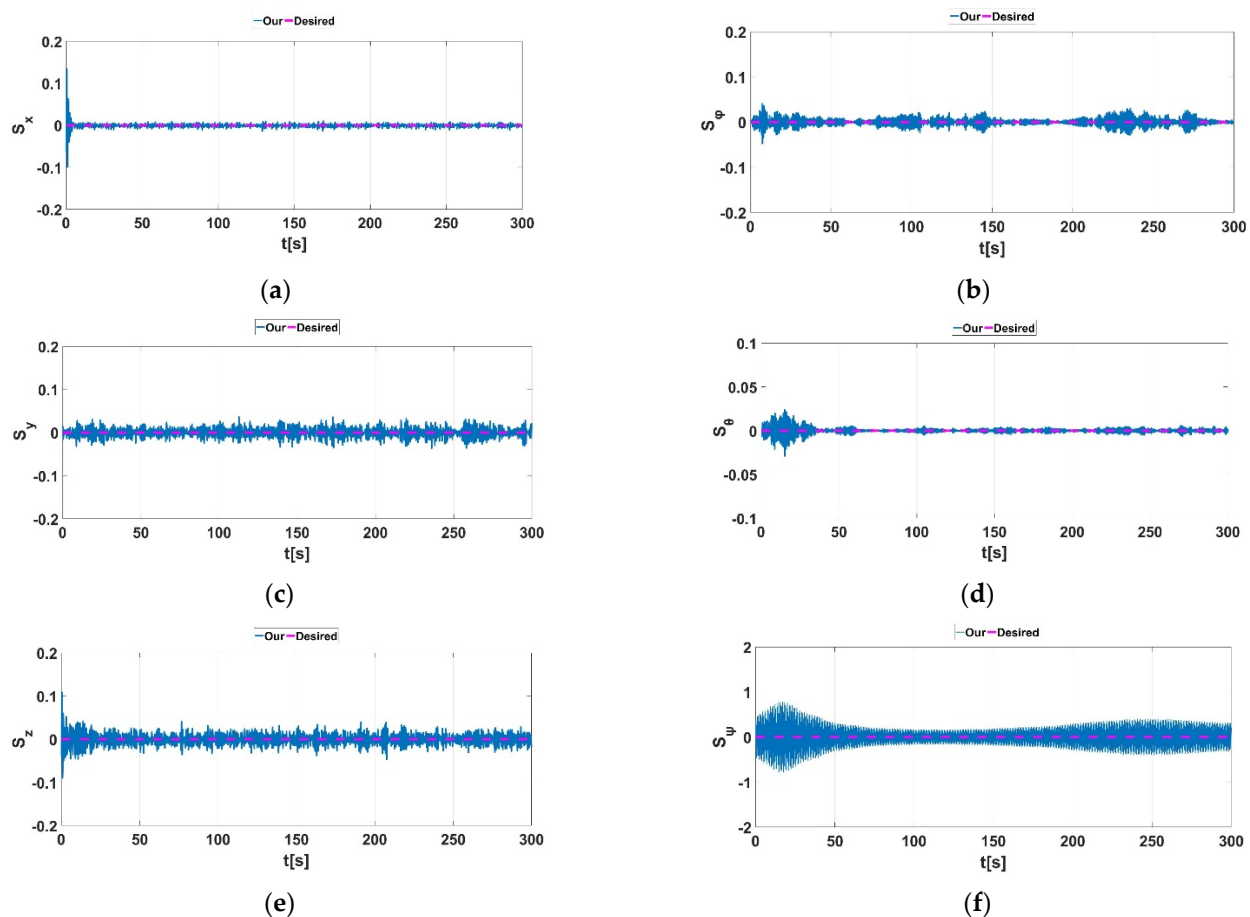
Figure 14. Inner−loop PID sliding surface $\boldsymbol{S}_{PID}$. (**a**) S_x; (**b**) S_φ; (**c**) S_y; (**d**) S_Θ; (**e**) S_z; (**f**) S_ψ.

　　　　To further verify the controller's performance, the disturbance of the ocean current was further increased on the basis of (72). The attack angle and sideslip angle of the current were $\alpha_c = rand(-1.57 \sim 1.57rad)$ and $\beta_c = rand(-3.14 \sim 3.14rad)$, respectively. Equation (71) shows that such random changes in the angle of attack and sideslip angle could make the linear velocity components of the ocean current on the three axes of the EF frame have positive and negative directions. The EF frame is shown in Figure 1. Then,

the current velocity was $V_c = rand(0\text{–}0.1 \text{ m/s})$ from 0 to 100 s, $V_c = rand(0\text{–}0.12 \text{ m/s})$ from 100 to 200 s, $V_c = rand(0\text{–}0.13 \text{ m/s})$ from 200 to 250 s, $V_c = rand(0\text{–}0.14 \text{ m/s})$ from 250 to 300 s, and $V_c = rand(0\text{–}0.15 \text{ m/s})$ from 300 s.
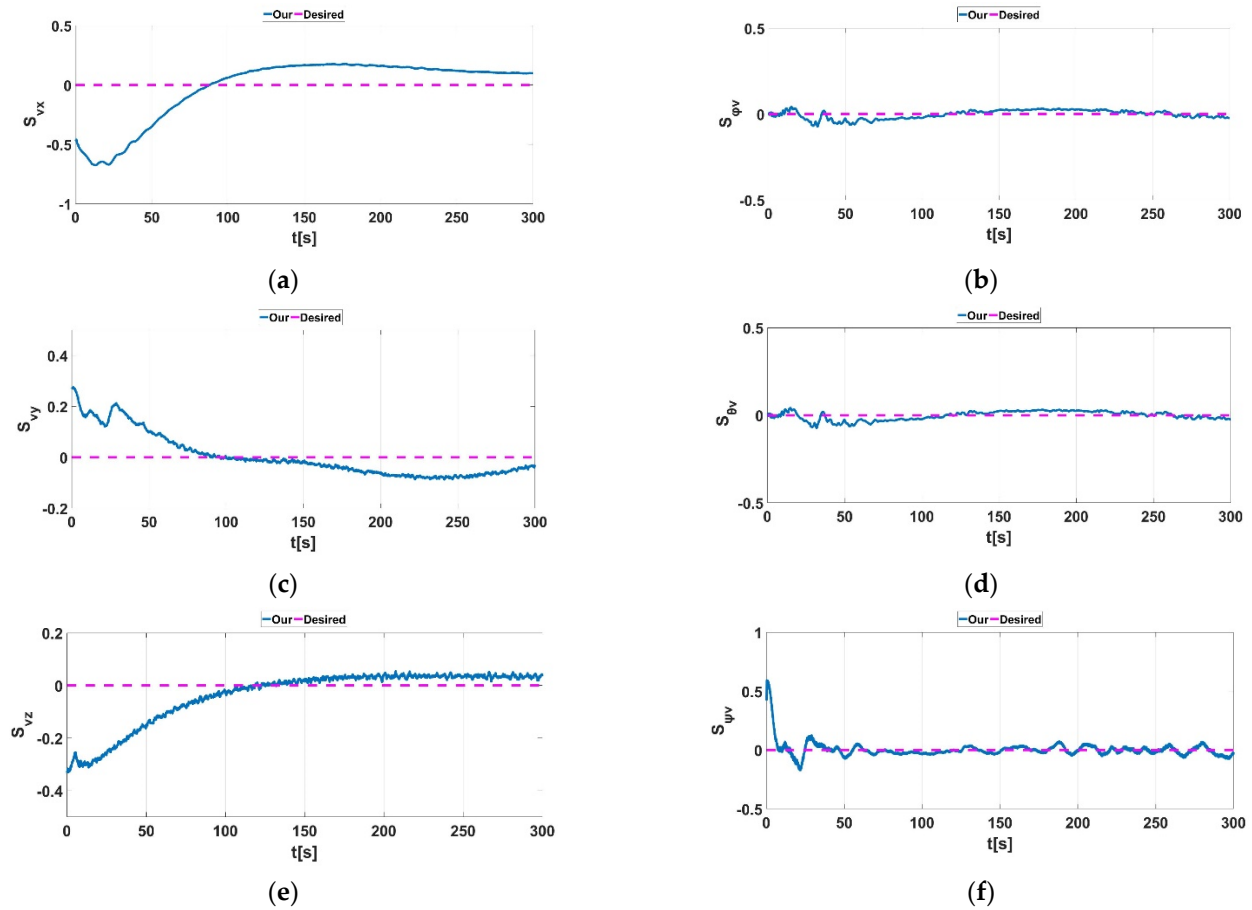
Figure 15. Outer−loop PID sliding surface $S_{\tilde{v}}$. (**a**) S_{vx}; (**b**) $S_{v\varphi}$; (**c**) S_{vy}; (**d**) $S_{v\Theta}$; (**e**) S_{vz}; (**f**) $S_{v\psi}$.

Figure 16 shows a 3D view of the underwater robot position tracking using the three control methods. The average values of D_E for the three methods are shown in Table 5.
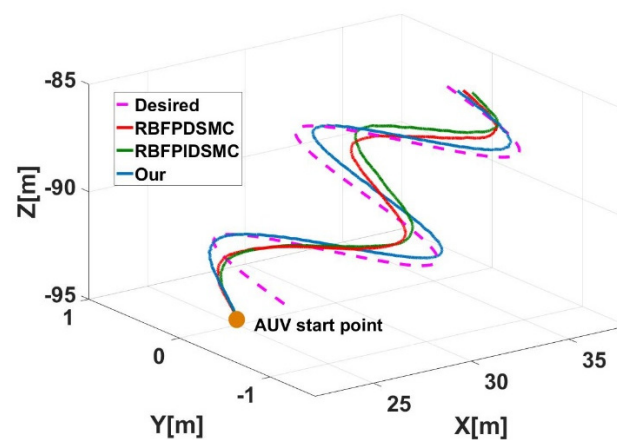
Figure 16. Three−dimensional view of the trajectory.

Table 5. Average values of D_E.

RBFPDSMC	RBFPIDSMC	DLNNSMC
0.54099	0.620367	0.285587

Table 5 shows that the average value of D_E for DLNNSMC was approximately 47.2% and 54.0% lower than that for RBFPDSMC and RBFPIDSMC, respectively. Figure 17 shows the position-tracking error. From the tracking results shown in these diagrams and tables, DLNNSMC exhibited a better tracking performance than the other two controllers under stronger interference. In addition, it exhibited a faster convergence rate and converged to a smaller range.
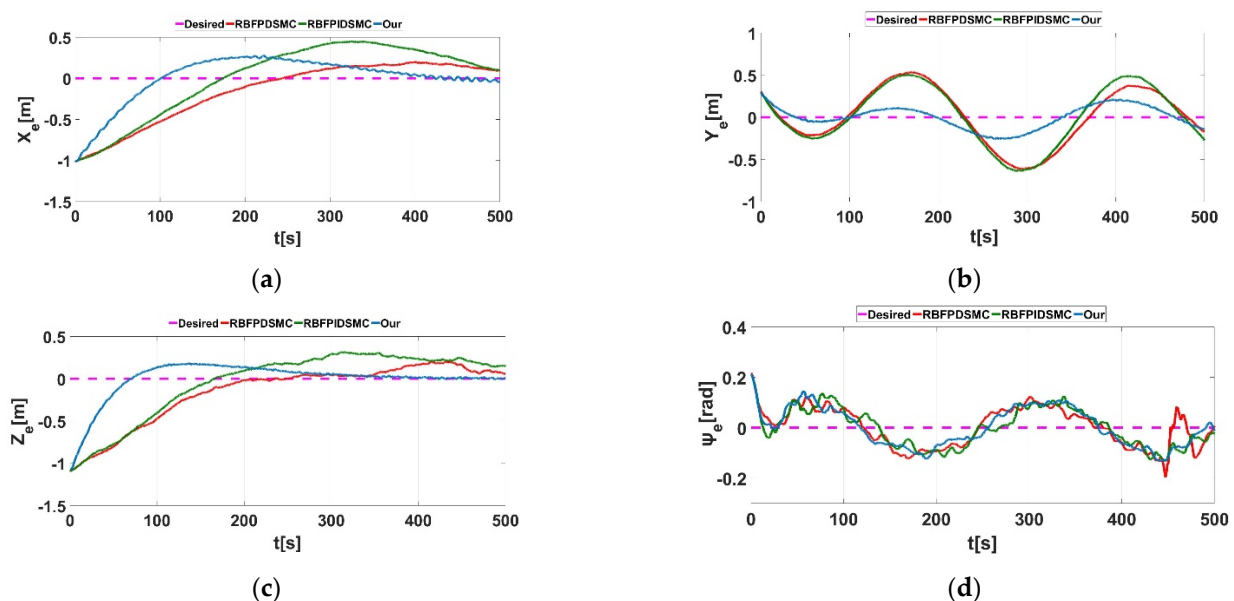
Figure 17. AUV position−tracking errors. (**a**) x_e; (**b**) y_e; (**c**) z_e; (**d**) ψ_e.

5. Discussion

This paper proposes a double-loop PID sliding mode surface, based on which DLNNSMC was designed by combining a nonlinear high-order observer with the RBF neural network. A trajectory-tracking control simulation experiment was carried out in an underwater simulation environment of Gazebo. Although the experimental results proved the effectiveness and superiority of DLNNSMC for trajectory tracking control under the influence of complex ocean currents, there are two aspects worth discussing. First, although our control method achieved good results in position-tracking error, there was some jitter in speed-tracking error. This is attributable to the design parameters and is worth studying in the future. Second, the control method could achieve a good convergence effect in the presence of strong ocean current effects; however, the convergence speed was slower, and the convergence range was larger. Therefore, this requires further research and discussion. A possible solution to the current implementation is to improve the nonlinear high-order observer and add reinforcement learning, adaptive law, and other algorithms. We will leave this problem of improving the robustness and stability of the controller to future work. In addition, we will try to apply the proposed control method to underactuated AUVs.

6. Conclusions

Here, we studied the trajectory tracking control problem of fully actuated AUVs with nonlinear disturbances. A new double-loop PID sliding surface is proposed to improve the convergence speed and robustness of the position- and velocity-tracking errors of an

ordinary PID sliding surface. Then, using this method, an adaptive control method for DLNNSMC is proposed. This method, combined with a nonlinear high-order observer and a neural network, could compensate for the uncertainty and unknown external disturbances of the model without an upper bound. Finally, DLNNSMC was compared with RBFPDSMC and RBFPIDSMC in two simulation experiments. Because DLNNSMC has two PID sliding surfaces that simultaneously tend to zero and compensate for the higher-order observer, the average value of D_E for DLNNSMC in the first experiment was 73.6% less than that for RBFPDSMC and 75.3% less than that for RBFPIDSMC. The average value of D_E for DLNNSMC in the second experiment was 86.8% less than that for RBFPDSMC and 88.8% less than that for RBFPIDSMC. Thus, the proposed method provides a faster convergence speed and a stronger robustness of position- and velocity-tracking errors. The effectiveness and superiority of this control method were verified in a more realistic simulation environment of Gazebo.

Author Contributions: Conceptualization, J.L. (Jiajian Liang) and F.Z.; methodology, J.L. (Jiajian Liang) and W.H.; software, J.L. (Jiaqiao Liang), J.L. (Jiajian Liang), X.Z., F.Z. and G.L. validation, G.L., E.X., J.L. (Jiajian Liang) and J.L. (Jiaqiao Liang); formal analysis, J.L. (Jiajian Liang), H.L. and X.Z.; investigation, G.L. and J.L. (Jiajian Liang); resources, J.L. (Jiajian Liang), F.Z. and E.X.; data curation, J.L. (Jiajian Liang), H.L., F.Z., G.L. and X.Z.; writing—original draft preparation, J.L. (Jiajian Liang); writing—review and editing, W.H.; visualization, J.L., J.L. (Jiaqiao Liang) and F.Z.; supervision, W.H.; project administration, W.H.; funding acquisition, W.H. All authors have read and agreed to the published version of the manuscript.

Institutional Review Board Statement: Not applicable.

Informed Consent Statement: Not applicable.

Data Availability Statement: Not applicable.

Conflicts of Interest: The authors declare no conflict of interest.

References

1. Sivčev, S.; Coleman, J.; Omerdić, E.; Dooly, G.; Toal, D. Underwater manipulators: A review. *Ocean Eng.* **2018**, *163*, 431–450. [CrossRef]
2. Zhao, C.; Thies, P.; Lars, J.; Cowles, J. ROV launch and recovery from an unmanned autonomous surface vessel–hydrodynamic modelling and system integration. *Ocean Eng.* **2021**, *232*, 109019. [CrossRef]
3. Gabl, R.; Davey, T.; Cao, Y.; Li, Q.; Li, B.; Walker, K.L.; Giorgio-Serchi, F.; Aracri, S.; Kiprakis, A.; Stokes, A.A.; et al. Hydrodynamic loads on a restrained ROV under waves and current. *Ocean Eng.* **2021**, *234*, 109279. [CrossRef]
4. Fu, M.; Wang, L. Finite-time coordinated path following control of underactuated surface vehicles based on event-triggered mechanism. *Ocean Eng.* **2022**, *246*, 110530. [CrossRef]
5. Kim, J.H.; Yoo, S.J. Adaptive event-triggered control strategy for ensuring predefined three-dimensional tracking performance of uncertain nonlinear underactuated underwater vehicles. *Mathematics* **2021**, *9*, 137. [CrossRef]
6. Kim, J.H.; Yoo, S.J. Nonlinear-observer-based design approach for adaptive event-driven tracking of uncertain underactuated underwater vehicles. *Mathematics* **2021**, *9*, 1144. [CrossRef]
7. Huang, W.; Zhou, F.; Zou, T.; Lu, P.; Xue, Y.; Liang, J.; Dong, Y. Alternating positive and negative feedback control model based on catastrophe theories. *Mathematics* **2021**, *9*, 2878. [CrossRef]
8. Jalving, B. The NDRE-AUV flight control system. *IEEE J. Ocean. Eng.* **1994**, *19*, 497–501. [CrossRef]
9. Kim, M.; Joe, H.; Pyo, J.; Kim, J.; Kim, H.; Yu, S.C. Variable-structure PID controller with anti-windup for autonomous underwater vehicle. In Proceedings of the 2013 OCEANS-San Diego (IEEE), San Diego, CA, 23–27 September 2013.
10. Do, K.D.; Jiang, Z.P.; Pan, J.; Nijmeijer, H. A global output-feedback controller for stabilization and tracking of underactuated ODIN: A spherical underwater vehicle. *Automatica* **2004**, *40*, 117–124. [CrossRef]
11. Pang, S.; Wang, J.; Liu, J.; Yi, H. Three-dimensional leader–follower formation control of multiple autonomous underwater vehicles based on line-of-sight measurements using the backstepping method. *Proc. Inst. Mech. Eng. Part I J. Syst. Control Eng.* **2018**, *232*, 819–829. [CrossRef]
12. Li, Y.; Wei, C.; Wu, Q.; Chen, P.; Jiang, Y.; Li, Y. Study of 3 dimension trajectory tracking of underactuated autonomous underwater vehicle. *Ocean Eng.* **2015**, *105*, 270–274. [CrossRef]

13. Chu, Z.; Xiang, X.; Zhu, D.; Luo, C.; Xie, D. Adaptive fuzzy sliding mode diving control for autonomous underwater vehicle with input constraint. *Int. J. Fuzzy Syst.* **2018**, *20*, 1460–1469. [CrossRef]

14. Wang, J.S.; Lee, C.G. Self-adaptive recurrent neuro-fuzzy control of an autonomous underwater vehicle. *IEEE Trans. Robot. Autom.* **2003**, *19*, 283–295. [CrossRef]

15. Kodogiannis, V.S. Neuro-control of unmanned underwater vehicles. *Int. J. Syst. Sci.* **2006**, *37*, 149–162. [CrossRef]

16. Zhang, L.J.; Qi, X.; Pang, Y.J. Adaptive output feedback control based on DRFNN for AUV. *Ocean Eng.* **2009**, *36*, 716–722. [CrossRef]

17. Seok Park, B. Neural network-based tracking control of underactuated autonomous underwater vehicles with model uncertainties. *J. Dyn. Syst. Meas. Control* **2015**, *137*, 021004. [CrossRef]

18. Cao, Y.; Li, B.; Li, Q.; Stokes, A.A.; Ingram, D.M.; Kiprakis, A. A nonlinear model predictive controller for remotely operated underwater vehicles with disturbance rejection. *IEEE Access* **2020**, *8*, 158622–158634. [CrossRef]

19. Zhao, Z.; He, X.; Ahn, C.K. Boundary disturbance observer-based control of a vibrating single-link flexible manipulator. *IEEE Trans. Syst. Man Cybern. Syst.* **2019**, *51*, 2382–2390. [CrossRef]

20. Zhao, Z.; He, X.; Ren, Z.; Wen, G. Boundary adaptive robust control of a flexible riser system with input nonlinearities. *IEEE Trans. Syst. Man Cybern. Syst.* **2018**, *49*, 1971–1980. [CrossRef]

21. Zhao, Z.; Ahn, C.K.; Li, H.X. Dead zone compensation and adaptive vibration control of uncertain spatial flexible riser systems. *IEEE ASME Trans. Mechatron.* **2020**, *25*, 1398–1408. [CrossRef]

22. Rangel, M.A.G.; Manzanilla, A.; Suarez, A.E.Z.; Muñoz, F.; Salazar, S.; Lozano, R. Adaptive non-singular terminal sliding mode control for an unmanned underwater vehicle: Real-time experiments. *Int. J. Control Autom. Syst.* **2020**, *18*, 615–628. [CrossRef]

23. Elmokadem, T.; Zribi, M.; Youcef-Toumi, K. Terminal sliding mode control for the trajectory tracking of underactuated autonomous underwater vehicles. *Ocean Eng.* **2017**, *129*, 613–625. [CrossRef]

24. Qiao, L.; Zhang, W. Adaptive second-order fast nonsingular terminal sliding mode tracking control for fully actuated autonomous underwater vehicles. *IEEE J. Ocean. Eng.* **2018**, *44*, 363–385. [CrossRef]

25. Hou, Q.; Ding, S. GPIO based super-twisting sliding mode control for PMSM. *IEEE Trans. Circuits Syst. II Express Briefs* **2020**, *68*, 747–751. [CrossRef]

26. Guerrero, J.; Torres, J.; Creuze, V.; Chemori, A. Adaptive disturbance observer for trajectory tracking control of underwater vehicles. *Ocean Eng.* **2020**, *200*, 107080. [CrossRef]

27. Zhihong, M.; Yu, X.H. Terminal sliding mode control of MIMO linear systems. *IEEE Trans. Circuits Syst. I Fundam. Theory Appl.* **1997**, *44*, 1065–1070. [CrossRef]

28. Wang, Y.; Gu, L.; Gao, M.; Zhu, K. Multivariable output feedback adaptive terminal sliding mode control for underwater vehicles. *Asian J. Control* **2016**, *18*, 247–265. [CrossRef]

29. Chen, Q.; Yang, Z.X. Adaptive RBF-PIDSMC control method with estimated model parameters for a piezo-actuated stage. *Microsyst. Technol.* **2021**, *27*, 69–77. [CrossRef]

30. Eftekhari Zadeh, E.; Feghhi, S.A.H.; Roshani, G.H.; Rezaei, A. Application of artificial neural network in precise prediction of cement elements percentages based on the neutron activation analysis. *Eur. Phys. J. Plus* **2016**, *131*, 167. [CrossRef]

31. Eftekhari-Zadeh, E.; Bensalama, A.S.; Roshani, G.H.; Salama, A.S.; Spielmann, C.; Iliyasu, A.M. Enhanced Gamma-Ray Attenuation-Based Detection System Using an Artificial Neural Network. *Photonics* **2022**, *9*, 382. [CrossRef]

32. Liu, C.; Wen, G.; Zhao, Z.; Sedaghati, R. Neural-network-based sliding-mode control of an uncertain robot using dynamic model approximated switching gain. *IEEE Trans. Cybern.* **2020**, *51*, 2339–2346. [CrossRef] [PubMed]